International Journal of Mechanical Sciences 313 (2026) 111329

Contents lists available at ScienceDirect

International Journal of Mechanical Sciences

journal homepage: www.elsevier.com/locate/ijmecsci

Growth-based shape control of hyperelastic plates under body forces

Zhanfeng Li [a], Xiaohu Yao [a,b], Mokarram Hossain [c], Jiong Wang [a,b,*]

[a] School of Civil Engineering and Transportation, South China University of Technology, Guangzhou, 510641, China
[b] State Key Laboratory of Subtropical Building and Urban Science, South China University of Technology, Guangzhou, 510641, China
[c] Zienkiewicz Institute for Modelling, Data and AI, Faculty of Science and Engineering, Swansea University, Swansea, SA1 8EN, United Kingdom

ARTICLE INFO

Keywords:
Nonlinear elasticity
Plate theory
Inverse problems
Differential growth
Body forces

ABSTRACT

Inspired by natural morphogenesis, controlling the shape of soft materials through differential growth has emerged as a strategy for developing smart devices. However, existing theoretical models typically neglect body forces (e.g., gravity), thereby restricting their applicability. Furthermore, mainstream inverse design methodologies rely on computational strategies, such as optimization and machine learning, but often lack mechanistic transparency compared to closed-form relations. To address these limitations, this study establishes a framework for shape control of hyperelastic plates that accounts for body forces. A key contribution of this work is the derivation of explicit asymptotic analytical solutions to the inverse problem. Unlike "black-box" numerical approaches, these solutions reveal quantitative relationships among applied body forces, required growth functions, and the geometric properties of the target shapes. We propose a shape-control framework that calculates analytical expressions of growth fields and designs appropriate loading paths to suppress structural instabilities. Our work demonstrates that body forces are not merely external loads but can also be harnessed as beneficial factors for shape morphing. The theoretical results are validated through three-dimensional finite element simulations and experiments on silicone plates under self-weight, demonstrating good agreement. This research provides mechanical insights and a design tool for morphing systems, extending the scope of soft robotics and deployable structures to scales where body forces are significant.

1. Introduction

Morphogenesis is a fundamental process describing how living organisms develop from embryonic forms to mature individuals. From microscopic cells to entire organisms, biological systems exhibit the capacity to grow by altering their mass and volume under specific conditions [1–3]. Growth is fundamental to life, enabling organisms to achieve complex 3D shapes and movements through spatially controlled expansion and contraction within soft tissues. Understanding and predicting growth-induced deformations remains challenging in biomechanics and growth mechanics, yet these efforts drive developments in materials science and engineering [4–7].

In recent decades, inspired by natural morphogenesis, shape control through growth has attracted increasing attention within the engineering community [8]. By prescribing local expansion or contraction, growth can be utilized to achieve target geometries and functions. This capability promotes progress in soft robotics, stimuli-responsive materials, and adaptive structures, facilitating the fabrication of components with predefined shapes and functionalities [9–13]. Recent advances demonstrate the broad applicability of shape memory polymers, ranging from self-coiling stents and origami grippers to magnetically responsive systems for remote actuation in soft robotics and biomedical devices [14–16]. Investigating how to achieve target shapes through prescribed growth fields not only deepens our understanding of biological morphogenesis but also supports the design of smart materials and devices.

Continuum mechanics provides a foundation for describing the morphological evolution of systems driven by differential growth. To model this process, we adopt the multiplicative decomposition of the total deformation gradient $\mathbb{F}$, which decomposes $\mathbb{F}$ into a growth tensor $\mathbb{G}$ and an elastic tensor $\mathbb{A}$, expressed as $\mathbb{F} = \mathbb{A}\mathbb{G}$. Kondaurov and Nikitin [17] and Takamizawa and Hayashi [18] originally introduced this concept. Their work predates the later formulation by Rodriguez et al. [19] by approximately a decade. For a detailed historical review of this decomposition in growth mechanics, we refer to Sadik and Yavari [20]. Through this decomposition, $\mathbb{G}$ encodes a virtual stress-free configuration, while $\mathbb{A}$ accounts for the elastic deformation required to enforce compatibility. When the imposed growth field is incompatible, it typically generates residual stresses that drive potential instabilities, such as creasing, wrinkling, and folding [21–23].

* Corresponding author at: School of Civil Engineering and Transportation, South China University of Technology, Guangzhou, 510641, China.
E-mail address: ctjwang@scut.edu.cn (J. Wang).

https://doi.org/10.1016/j.ijmecsci.2026.111329
Received 15 September 2025; Received in revised form 5 January 2026; Accepted 29 January 2026
Available online 2 February 2026
0020-7403/© 2026 Elsevier Ltd. All rights are reserved, including those for text and data mining, AI training, and similar technologies.

Although the full 3D continuum formulation offers a general framework, its direct application to thin structures, such as leaves, petals, or engineered membranes, can be computationally prohibitive and may obscure key mechanisms. For plate structures of small thickness, developing reduced models is both natural and advantageous. Therefore, plate theories are required to describe the growth-induced deformation of such samples. Within the framework of finite strain, existing plate theories can be broadly grouped into (i) the extended Föppl-von Kármán (EFvK) models [24], (ii) the Koiter-based models [25], and (iii) the consistent finite-strain plate models [26]. The first two models rely on *a priori* hypotheses motivated by engineering intuition, which may compromise accuracy outside the range of those assumptions [27]. To capture general responses, employing formulations that are asymptotically consistent with the 3D weak form to a certain order is necessary. Dai and Song [26] derived such a plate theory from the 3D governing system through a series expansion and truncation method. To incorporate growth effects, Wang et al. [28] extended the consistent finite-strain plate model using the multiplicative decomposition and applied it to multilayer plates [29]. Furthermore, dynamic behaviours such as transverse vibrations in plates with defects have also been extensively studied [30]. Despite their asymptotic consistency, the resulting plate equations are strongly nonlinear. Consequently, closed-form analytical solutions are usually inaccessible except in ideal or symmetric settings. Other models, such as non-Euclidean plate models [31,32] and Cosserat plate models [33,34], also provide valuable perspectives, although they are not detailed herein.

Parallel to the development of growth theories, the fundamental mechanics of slender structures under body forces (classically known as the "heavy elastica" problem [35]) has seen renewed interest. Distributed body forces are now understood to fundamentally reshape equilibrium branches and stability limits, effects that become even more pronounced in extreme environments like supergravity [36]. Recent theoretical advances have extended this understanding to complex scenarios, establishing the heavy elastica as a benchmark for validating numerical simulators [37] and exploring force control applications [38]. Notably, in constrained systems, gravity has been shown to induce rich bifurcation behaviours, such as mode switching in confined rods [39] and critical slipping thresholds between supports [40]. In the context of hyperelasticity, Azarniya et al. [41] revealed that strain-stiffening significantly alters post-buckling responses under self-weight. Collectively, these studies highlight the non-trivial role of body forces in structural mechanics, underscoring the necessity of incorporating them into the theoretical modelling of morphing plates.

Driven by the rising demand for programmable materials, researchers have shifted attention from predicting sample responses with prescribed growth fields to solving the inverse problem. The inverse problem seeks growth fields that drive a body towards a specified target shape and is fundamental to developments in soft robotics, adaptive biomedical devices, and biomimetic morphing structures [42–44]. Considerable progress has been achieved through both numerical and analytical approaches. Numerical optimization enables the treatment of complex geometries and strong nonlinearities. For example, van Rees et al. [45] combined variational optimization with finite elements to determine incompatible strain fields that morph flat plates into 3D surfaces. Ortigosa-Martínez et al. [46] implemented gradient-based optimization frameworks for hyperelastic plates that incorporate differential growth. Bertails-Descoubes et al. [47] addressed the inverse problem for suspended Kirchhoff rods subject to gravitational loading using a numerical framework. To improve computational efficiency, Chen et al. [48] proposed an asymptotic numerical method for inverse design that significantly accelerates convergence compared to traditional Newton-type methods. More recently, physics-informed neural networks (PINNs) and related physics-informed machine-learning approaches have emerged as a mesh-free paradigm for inverse design. Luo et al. [49] provided a comprehensive review of PINNs for solving PDE inverse problems, highlighting the challenges of handling boundary conditions through constraints. Ahmed et al. [50] utilized a data-driven methodology to assess structural performance, concluding that geometry-aware material placement is more effective for deformation control than simply increasing mass. While these methods are powerful, they often lack physical interpretability [51]. As noted by Han et al. [52] and Feng et al. [53], although AI-driven design is efficient, establishing explicit physical relationships remains crucial for understanding the underlying mechanisms. In this context, our analytical approach complements these computational tools by providing analytical solutions that satisfy boundary conditions and reveal the direct dependence of growth fields on geometric parameters.

Apart from numerical methods, analytical approaches have yielded explicit expressions for growth functions for arbitrary target shapes under stress-free conditions. Wang, Li, and co-workers [54–57] derived explicit growth functions for hyperelastic plates and shells to realize broad families of target shapes (including topology changes and conformal and isometric mappings) in stress-free settings. Chen et al. [58] likewise derived analytical solutions generating complex fold morphologies. Li et al. [59] developed a theory-assisted optimization design framework for morphing slender structures, bypassing the computational cost of optimization-based methods. Similar to the present study, analytical reviews in other fields, such as heat transfer in functionally graded materials [60,61], have also highlighted the value of analytical solutions for understanding complex physical behaviours. Such analytical inverse-design results provide explicit and mechanistically interpretable mappings from geometry to programmed fields, enable rapid parametric exploration at negligible computational cost, and serve as physics-consistent baselines for validating or guiding inverse solvers [49,51]. To clearly position the present study within this landscape and highlight the lack of frameworks addressing body forces, we summarize representative works in Table 1.

As illustrated in Table 1, despite considerable advances in growth-based shape control of soft materials, many existing studies rely on numerical optimization, thereby lacking the mechanistic transparency of analytical solutions. Furthermore, the majority of these works neglect the influence of body forces. However, body forces are ubiquitous and can be dominant across various scales. In micro-gravity environments, Lü et al. [62] highlighted that gravity-induced instabilities can be harnessed to create programmable surface patterns. Conversely, in soft robotics, the gravity effect (sagging under self-weight) poses a challenge for large-scale actuators. Recent works have explored inverse design strategies to compensate for these effects, such as pre-cambering pneumatic actuators to account for gravity [63], incorporating inertial body forces into dynamic control loops [64], or harvesting energy from gravity-induced vibrations [65]. This omission in classical growth theories, particularly the absence of analytical solutions accounting for body forces, confines their applicability to small, lightweight specimens and misses the opportunity to exploit body forces as integral design variables. Therefore, developing analytical frameworks that incorporate body forces is not only crucial for growth theory but also enables novel design strategies for material engineering.

To address current research gaps, this study develops a growth-based shape-control framework for hyperelastic plane-strain plates subjected to body forces. Specifically, we aim to (i) establish a nonlinear plate model that incorporates both differential growth and body forces; (ii) derive analytical relations between the geometric properties of target shapes, body forces, and the required growth fields; and (iii) validate the framework through numerical simulations and experiments. This work bridges biology and engineering, offering insights into the responses of morphoelastic plates under body forces and enabling shape control under such conditions. Compared with numerical optimization methods, our analytical results are interpretable and computationally efficient. The proposed framework provides a basis for large-scale soft robotics, deployable morphing structures, and bio-inspired morphogenesis.

Table 1
Comparison of representative studies on growth-induced deformation and shape control.

Reference	Focus	Object	Methodology	Growth	Body forces
Dai and Song [26]	Forward	Plates	Analytical analysis	No	No
Wang et al. [28]	Forward	Plates	Analytical analysis	Yes	No
van Rees et al. [45]	Inverse	Bilayers	Numerical optimization	Yes	No
Wang et al. [54]	Inverse	Plates	Analytical analysis	Yes	No
Bertails-Descoubes et al. [47]	Inverse	Rods	Numerical optimization	No	Yes (Gravity)
Ortigosa-Martínez et al. [46]	Inverse	3D solids	Numerical optimization	Yes	No
Present work	Inverse	Plates	Analytical analysis	Yes	Yes (Generic)

The paper is outlined as follows: Section 2 formulates the nonlinear plane-strain plate model with multiplicative growth under body forces and derives the plate equation system. Section 3 develops the inverse (shape-control) framework, obtains asymptotic analytical growth functions, and verifies them through finite-element simulations for uniform and spatially varying body forces and target shapes (flat, semicircle, parabola, and spiral). Section 4 presents experimental validation using pre-strained silicone plates under self-weight. Section 6 summarizes the key findings, discusses limitations, and suggests future research directions.

2. Nonlinear model for a plane-strain plate of growth under body forces

In this section, we develop a nonlinear model to describe the large deformation of a hyperelastic plane-strain plate under the combined influence of differential growth and body forces. Our model is based on the framework of finite-strain continuum mechanics. We first establish the kinematics of the plate, then derive the 3D governing system, and finally obtain the plate equation.

2.1. Kinematics and the modelling of growth effects

We consider a 3D hyperelastic plate with constant thickness, the cross-section of which is depicted in Fig. 1. In its reference configuration, denoted by $\mathcal{K}_r$, the plate occupies the cuboid domain

$$\mathcal{K}_r = \{(X, Y, Z) \mid 0 < X < L,\ 0 < Y < W,\ 0 < Z < 2h\}, \tag{1}$$

where L denotes the length of the plate, W is the width, and $2h$ is the total thickness. By defining a Cartesian coordinate system $\{O; \mathbf{e}_1, \mathbf{e}_2, \mathbf{e}_3\}$, the position vector of a material point in $\mathcal{K}_r$ is given by $\mathbf{X} = X\mathbf{e}_1 + Y\mathbf{e}_2 + Z\mathbf{e}_3$. Here, the basis vector $\mathbf{e}_1$ aligns with the plate's longitudinal bottom surface, $\mathbf{e}_2$ represents the width direction, and $\mathbf{e}_3$ aligns with the thickness direction. We consider the plate to be subjected to a distributed body force per unit volume in the reference configuration $\mathcal{K}_r$, denoted by $\mathbf{b}_r = b_{r1}\mathbf{e}_1 + b_{r3}\mathbf{e}_3$. This body force represents any non-contact force acting on the bulk of the material. A typical example of such a force is gravity, in which case $\mathbf{b}_r = \rho_r \mathbf{g}$, where ρ_r denotes the initial material density and $\mathbf{g}$ is the gravitational acceleration vector. In the context of the shape-control framework presented here, we assume that the structure maintains a fixed operational orientation relative to the external field. Consequently, $\mathbf{b}_r$ is treated as a prescribed, time-independent vector field determined by this specific posture. Addressing the varying components of body forces resulting from dynamic changes in attitude requires real-time adaptive strategies and is beyond the scope of static analysis. Due to external forces and growth effects, the plate reaches a current configuration $\mathcal{K}_t$. The position vector of a material point in $\mathcal{K}_t$ is denoted by $\mathbf{x} = x\mathbf{e}_1 + y\mathbf{e}_2 + z\mathbf{e}_3$. We then apply the plane-strain assumption ($y = Y,\ \partial x/\partial Y = 0,\ \partial z/\partial Y = 0$). While soft robotic structures often exhibit complex three-dimensional deformations, this assumption is adopted here to reduce the dimensionality of the problem, thereby enabling the derivation of explicit analytical solutions. These closed-form solutions are essential for revealing the quantitative mechanistic relationship between growth, body forces, and target shapes, which might be obscured in a fully numerical 3D analysis. Physically, this setting corresponds to wide plate structures or soft actuators where lateral expansion is constrained, for instance, by clamping or by embedding high-modulus fibres along the width direction. Under this assumption, the deformation gradient tensor $\mathbb{F}$ can be calculated as

$$\mathbb{F} = \frac{\partial \mathbf{x}}{\partial \mathbf{X}} = \frac{\partial x}{\partial X}\mathbf{e}_1 \otimes \mathbf{e}_1 + \frac{\partial x}{\partial Z}\mathbf{e}_1 \otimes \mathbf{e}_3 + \mathbf{e}_2 \otimes \mathbf{e}_2 + \frac{\partial z}{\partial X}\mathbf{e}_3 \otimes \mathbf{e}_1 + \frac{\partial z}{\partial Z}\mathbf{e}_3 \otimes \mathbf{e}_3, \tag{2}$$

where the tensor product $\mathbf{e}_i \otimes \mathbf{e}_j$ constructs a second-order tensor.

A foundational assumption of growth theory is the multiplicative decomposition of the total deformation gradient $\mathbb{F}$ into an elastic part $\mathbb{A}$ and a growth part $\mathbb{G}$ [66]. This relationship is expressed as

$$\mathbb{F} = \mathbb{A}\mathbb{G}, \tag{3}$$

where the growth tensor $\mathbb{G}$ encodes a virtual stress-free configuration that is sometimes incompatible, in the sense that a global stress-free configuration may not exist. The elastic tensor $\mathbb{A}$ then accommodates this growth field by introducing the necessary elastic deformation to ensure the body's continuity. Consequently, if the growth field is incompatible (i.e., the compatibility condition $\nabla \times \mathbb{G} \neq \mathbf{0}$ is not satisfied), it generates internal residual stresses even in the absence of external loads [67,68].

We consider a quasi-static growth process, given that biological growth is typically much slower than elastic wave propagation [69,70]. This quasi-static assumption allows the problem to be formulated as a sequence of boundary-value problems rather than a dynamic one, simplifying the subsequent analysis. Since this work considers a quasi-static growth process, we prescribe this time-independent growth field as a function of the material coordinate $\mathbf{X}$.

For shape-control purposes, we prescribe a growth field capable of inducing both axial extension/shrinkage and bending. The growth tensor $\mathbb{G}$ is characterized by diagonal growth functions, λ_i, which quantify the local stretch/compression ratio along directions $\mathbf{e}_i$. For the plane-strain plate considered here, we prescribe a growth field designed to induce desired deformations efficiently. While growth in biological systems and engineered materials is often volumetric and occurs simultaneously along multiple axes (width and thickness), we restrict our formulation to growth along the longitudinal axis $\mathbf{e}_1$ with a linear variation through the thickness coordinate Z. This restriction is a strategic choice for efficiency rather than a limitation of the framework's capability. For the plane-strain plate considered in this study, the longitudinal growth function and its through-thickness gradient provide sufficient degrees of freedom to control the arc length and curvature, respectively, allowing for the realization of arbitrary smooth shapes [71]. Introducing simultaneous growth in the width and thickness directions would increase the complexity of both the theoretical inverse problem (leading to non-unique solutions) and the physical implementation, without expanding the achievable solution space for these structures. If multidirectional growth is required for other applications, the formulation can be extended by incorporating the corresponding growth tensor components. Consequently, we assume no growth in the width direction ($\lambda_2 = 1$), consistent with the plane-strain constraint, and set $\lambda_3 = 1$ to preserve analytical tractability. The growth tensor is thus defined as

$$\mathbb{G} = \lambda_1(X, Z)\mathbf{e}_1 \otimes \mathbf{e}_1 + \mathbf{e}_2 \otimes \mathbf{e}_2 + \mathbf{e}_3 \otimes \mathbf{e}_3, \tag{4}$$

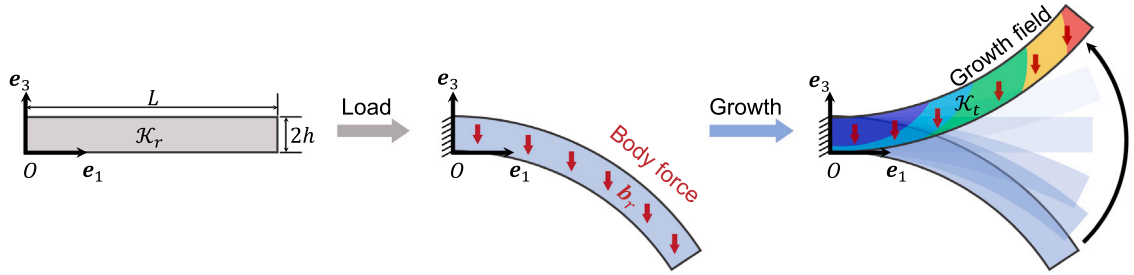


Fig. 1. Kinematics of the plane-strain plate. The reference configuration $\mathcal{K}_r$ (left) is a plate of length L and thickness $2h$, subjected to a body force $\mathbf{b}_r$. The current configuration $\mathcal{K}_t$ (right) results from the combined effects of body forces and growth field.

where the growth function $\lambda_1(X,Z)$ is given by

$$\lambda_1(X,Z)=\lambda_1^{(0)}(X)+Z\lambda_1^{(1)}(X). \tag{5}$$

Here, $\lambda_1^{(0)}$ is the growth function of the bottom surface, representing local extension or contraction, and $\lambda_1^{(1)}$ is the growth gradient along the thickness, which programs the plate's curvature. The identification of $\{\lambda_1^{(0)},\lambda_1^{(1)}\}$ for arbitrary desired target shapes under body forces is the central goal of this work.

To describe the elastic response of a material incorporating growth effects, the elastic strain energy function is defined as

$$\Psi_e(\mathbb{F},\mathbb{G})=J_G\Psi_0(\mathbb{A})=J_G\Psi_0(\mathbb{F}\mathbb{G}^{-1}), \tag{6}$$

where $J_G=\operatorname{Det}\mathbb{G}$. Eq. (6) provides flexibility in choosing the hyperelastic model, allowing Ψ_0 to represent various constitutive models such as neo-Hookean, Mooney–Rivlin, Gent, Ogden, etc. Hossain and Steinmann [72] and Mihai et al. [73].

Soft biological tissues, composed largely of water-based matrices, exhibit a high ratio of bulk to shear modulus within physiological deformation ranges, justifying the incompressibility assumption [74]. Furthermore, typical hyperelastic materials used for experimental validation, such as silicone elastomers and rubbers, possess a Poisson ratio ν approaching 0.5 (typically $\nu\approx 0.499$). This incompressibility can be mathematically expressed through the following constraint equation

$$\mathcal{R}(\mathbb{F},\mathbb{G})=J_G R_0(\mathbb{A})=J_G\left(J_A-1\right)=0, \tag{7}$$

where $J_A=\operatorname{Det}\mathbb{A}$. In this study, we adopt the incompressible neo-Hookean model primarily to facilitate the derivation of analytical solutions for the inverse problem. Its elastic strain–energy function is $\Psi_0=C_0\left[\operatorname{tr}\left(\mathbb{A}\mathbb{A}^{\mathrm{T}}\right)-3\right]$, where C_0 is the material constant (half of the shear modulus). The nominal stress tensor $\mathbb{S}$ for an incompressible hyperelastic solid with growth effects can then be calculated through the constitutive relation

$$\mathbb{S}=\frac{\partial\Psi_e(\mathbb{F},\mathbb{G})}{\partial\mathbb{F}}-p\frac{\partial\mathcal{R}(\mathbb{F},\mathbb{G})}{\partial\mathbb{F}}=J_G\mathbb{G}^{-1}\left(2C_0\mathbb{A}^{\mathrm{T}}-p(\mathbf{X})\mathbb{A}^{-1}\right), \tag{8}$$

where $p(\mathbf{X})$ is the Lagrange multiplier (representing the hydrostatic pressure) associated with the incompressibility constraint (7).

During the shape morphing process, the hyperelastic plate should satisfy the mechanical equilibrium equation

$$\operatorname{Div}\mathbb{S}+\mathbf{b}_r=\mathbf{0},\ \text{in}\ \mathcal{K}_r. \tag{9}$$

To render the equilibrium problem well-defined, Eq. (9) should be complemented by appropriate boundary conditions. For a cantilever plate clamped at $X=0$, the displacement and orientation are fixed. For the free end at $X=L$, the surface traction is zero. On the top and bottom surfaces, there are no surface tractions. The boundary conditions are summarized as follows

$$\begin{cases} x=0 \text{ and } z=Z,\ \text{on}\ X=0,\\ \mathbb{S}^{\mathrm{T}}\mathbf{e}_1=\mathbf{0},\ \text{on}\ X=L,\\ \mathbb{S}^{\mathrm{T}}\mathbf{e}_3=\mathbf{0},\ \text{on}\ Z=0,2h. \end{cases} \tag{10}$$

The mechanical equilibrium equation (9), the incompressibility constraint (7), and the boundary conditions (10) constitute a nonlinear 3D governing system for the plate, with unknowns $\{\mathbf{x},p\}$.

2.2. Derivation of the plate equation

To simplify the problem governed by PDEs (Eqs. (7), (9), (10)) into a more tractable system of ODEs, we derive an equation system for the plate. This reduces the independent spatial variables from $\{X,Z\}$ to a single variable X, a standard practice for slender bodies.

Our derivation follows the series expansion and truncation method, similar to that used for finite-strain plates [26,28]. We begin by expanding the position vector $\mathbf{x}$, the hydrostatic pressure p, and the body force $\mathbf{b}_r$ as Taylor series expansions in the thickness coordinate Z on the bottom surface. Considering terms of sufficient order to capture the plate's mechanical response, we have

$$\begin{aligned} \mathbf{x}(X,Z)&=\mathbf{x}^{(0)}(X)+Z\mathbf{x}^{(1)}(X)+\frac{1}{2}Z^2\mathbf{x}^{(2)}(X)+\frac{1}{6}Z^3\mathbf{x}^{(3)}(X)+O(Z^4),\\ p(X,Z)&=p^{(0)}(X)+Zp^{(1)}(X)+\frac{1}{2}Z^2p^{(2)}(X)+O(Z^3),\\ \mathbf{b}_r(X,Z)&=\mathbf{b}_r^{(0)}(X)+Z\mathbf{b}_r^{(1)}(X)+\frac{1}{2}Z^2\mathbf{b}_r^{(2)}(X)+O(Z^3), \end{aligned} \tag{11}$$

where $\mathbf{x}^{(n)}(X)$ and $p^{(n)}(X)$ are unknown functions of X. This expansion allows us to express the position vector $\mathbf{x}$ and pressure p across the thickness in terms of the bottom surface $\mathbf{x}^{(0)}$. By substituting these expansions (11) into the deformation gradient $\mathbb{F}$, the elastic deformation tensor $\mathbb{A}$, and the nominal stress tensor $\mathbb{S}$, we obtain

$$\begin{aligned} \mathbb{F}&=\mathbb{F}^{(0)}+Z\mathbb{F}^{(1)}+\frac{1}{2}Z^2\mathbb{F}^{(2)}+O(Z^3),\\ \mathbb{A}&=\mathbb{A}^{(0)}+Z\mathbb{A}^{(1)}+\frac{1}{2}Z^2\mathbb{A}^{(2)}+O(Z^3),\\ \mathbb{S}&=\mathbb{S}^{(0)}+Z\mathbb{S}^{(1)}+\frac{1}{2}Z^2\mathbb{S}^{(2)}+O(Z^3). \end{aligned} \tag{12}$$

Next, by substituting $\mathbb{A}=\mathbb{F}\mathbb{G}^{-1}$ into the constitutive relation (8), one can derive expressions for $\mathbb{S}^{(0)}$, $\mathbb{S}^{(1)}$, and $\mathbb{S}^{(2)}$. From the mechanical equilibrium equation (9), we obtain the following relations by collecting coefficients at each order in Z

$$\left(\frac{\partial S_{11}^{(n)}}{\partial X}+S_{31}^{(n+1)}\right)\mathbf{e}_1+\left(\frac{\partial S_{13}^{(n)}}{\partial X}+S_{33}^{(n+1)}\right)\mathbf{e}_3+\mathbf{b}_r^{(n)}=\mathbf{0}, \tag{13}$$

where $S_{ij}^{(n)}$ are the components of $\mathbb{S}^{(n)}$, and n runs from 0 to 1, which is sufficient for this work to realize complex shape programming. In fact, if the expansion (11) contains higher-order terms, relation (13) also holds for them.

We substitute (11) into the constraint (7), the mechanical equilibrium (9), and the boundary condition $(10)_3$ at $Z=0$. By equating the coefficients of Z^0, Z^1, and Z^2 in Eq. (7) to zero, those of Z^0 and Z^1 in Eq. (9) to zero, and the coefficient of Z^0 in Eq. $(10)_3$ to zero, we formulate a closed linear system for the iterative higher-order unknowns $\{\mathbf{x}^{(1)},\mathbf{x}^{(2)},\mathbf{x}^{(3)},p^{(0)},p^{(1)},p^{(2)}\}$ in terms of $\mathbf{x}^{(0)}$.

Following the procedures in [54], we introduce the following geometric quantities to simplify the lengthy expressions of the higher-order unknowns

$$\begin{aligned} &\mathbf{r}=x^{(0)}\mathbf{e}_1+z^{(0)}\mathbf{e}_3,\quad \mathbf{r}_n=\mathbf{r}'\times\mathbf{e}_2,\\ &E_r=\mathbf{r}'\cdot\mathbf{r}',\quad L_r=\frac{\mathbf{r}''\cdot\mathbf{r}_n}{\sqrt{E_r}}, \end{aligned} \tag{14}$$

where $'$ denotes the derivative with respect to X, and $\mathbf{r}'$ and $\mathbf{r}_n$ are the tangent and normal vectors on the bottom of the plate, respectively. E_r and L_r are the coefficients of the first and second fundamental forms of the surface $\mathbf{r}$. The higher-order unknowns can then be expressed as follows ($\{\mathbf{x}^{(3)}, p^{(2)}\}$ are omitted for brevity but can be derived using `Mathematica`):

$$\begin{aligned}
\mathbf{x}^{(1)} =& \frac{\lambda_1^{(0)}}{E_r}\mathbf{r}_n, \quad p^{(0)} = \frac{2C_0{\lambda_1^{(0)}}^2}{E_r},\\
\mathbf{x}^{(2)} =& -\frac{\mathbf{b}_r^{(0)}}{2C_0\lambda_1^{(0)}} + \left[\frac{\mathbf{b}_r^{(0)}\cdot\mathbf{r}_n}{2C_0E_r\lambda_1^{(0)}} + \frac{L_r\left({E_r}^2+3{\lambda_1^{(0)}}^4\right)}{{E_r}^{5/2}{\lambda_1^{(0)}}^2} + \frac{\lambda_1^{(1)}}{E_r}\right]\mathbf{r}_n\\
&+ \frac{\left({E_r}^2+2{\lambda_1^{(0)}}^4\right)\lambda_1^{(0)\prime}}{{E_r}^2{\lambda_1^{(0)}}^3}\mathbf{r}' - \frac{{E_r}^2+2{\lambda_1^{(0)}}^4}{{E_r}^2{\lambda_1^{(0)}}^2}\mathbf{r}'',\\
p^{(1)} =& \frac{\mathbf{b}_r^{(0)}\cdot\mathbf{r}_n}{E_r} + \frac{2C_0L_r\left({E_r}^2+{\lambda_1^{(0)}}^4\right)}{{E_r}^{5/2}\lambda_1^{(0)}} + \frac{4C_0\lambda_1^{(0)}\lambda_1^{(1)}}{E_r}.
\end{aligned} \tag{15}$$

By virtue of the iteration relations in Eq. (15), the nominal stress tensor $\mathbb{S}$ can also be expressed in terms of $\mathbf{x}^{(0)}$ ($\mathbb{S}^{(2)}$ is omitted for brevity)

$$\begin{aligned}
\mathbb{S}^{(0)} =& 2C_0\left[\frac{{E_r}^2-{\lambda_1^{(0)}}^4}{{E_r}^2\lambda_1^{(0)}}\mathbf{e}_1\otimes\mathbf{r}' + \frac{\lambda_1^{(0)}\left(E_r-{\lambda_1^{(0)}}^2\right)}{E_r}\mathbf{e}_2\otimes\mathbf{e}_2\right],\\
\mathbb{S}^{(1)} =& \mathbf{e}_1\otimes\left[-\frac{\lambda_1^{(0)}}{E_r}\mathbf{b}_r^{(0)}\times\mathbf{e}_2 - \frac{4C_0\lambda_1^{(0)}\left({E_r}^2+{\lambda_1^{(0)}}^4\right)}{{E_r}^3}\left(\frac{\mathbf{r}_n}{\lambda_1^{(0)}}\right)'\right.\\
&\left.-\left(\frac{2\mathbf{b}_r^{(0)}\cdot\mathbf{r}_n\lambda_1^{(0)}}{{E_r}^2} + 2C_0\left(\frac{\lambda_1^{(1)}\left({E_r}^2+3{\lambda_1^{(0)}}^4\right)}{{E_r}^2{\lambda_1^{(0)}}^2} + \frac{4L_r\left({E_r}^2+{\lambda_1^{(0)}}^4\right)}{{E_r}^{7/2}}\right)\right)\mathbf{r}'\right]\\
&-\left(\frac{1}{E_r}\left(\mathbf{b}_r^{(0)}\cdot\mathbf{r}_n\lambda_1^{(0)} + 2C_0\left(L_r\sqrt{E_r}-\lambda_1^{(1)}\left(E_r-3{\lambda_1^{(0)}}^2\right)+\frac{L_r{\lambda_1^{(0)}}^4}{{E_r}^{3/2}}\right)\right)\right)\mathbf{e}_2\otimes\mathbf{e}_2\\
&-\mathbf{e}_3\otimes\left[\mathbf{b}_r^{(0)} - \frac{8C_0L_r{\lambda_1^{(0)}}^3}{{E_r}^{5/2}}\mathbf{r}_n + \frac{2C_0\left({E_r}^2+3{\lambda_1^{(0)}}^4\right)}{{E_r}^2}\left(\frac{\mathbf{r}'}{\lambda_1^{(0)}}\right)'\right].
\end{aligned} \tag{16}$$

Finally, by subtracting the top and bottom traction-free boundary conditions given in Eq. $(10)_3$ and using the relation in Eq. (13), we obtain the following 2D plate equation

$$\frac{\partial\bar{S}_{11}}{\partial X}\mathbf{e}_1 + \frac{\partial\bar{S}_{13}}{\partial X}\mathbf{e}_3 + \bar{\mathbf{b}}_r = \mathbf{0}, \tag{17}$$

where $\bar{\mathbb{S}}$ and $\bar{\mathbf{b}}_r$ are the average stress and body force over the thickness of the plate, i.e.,

$$\begin{aligned}
\bar{\mathbb{S}} &= \frac{1}{2h}\int_0^{2h}\mathbb{S}\,\mathrm{d}Z = \mathbb{S}^{(0)} + h\mathbb{S}^{(1)} + \frac{2h^2}{3}\mathbb{S}^{(2)},\\
\bar{\mathbf{b}}_r &= \frac{1}{2h}\int_0^{2h}\mathbf{b}_r\,\mathrm{d}Z = \mathbf{b}_r^{(0)} + h\mathbf{b}_r^{(1)} + \frac{2h^2}{3}\mathbf{b}_r^{(2)}.
\end{aligned} \tag{18}$$

For predicting the deformation of a plate with given growth fields and body forces, Eq. (17) provides two equations for the two unknowns $x^{(0)}$ and $z^{(0)}$. To complete the system, we propose boundary conditions based on the original boundary conditions (10) in the 2D problem, ensuring consistency.

$$\begin{aligned}
&\bar{\mathbb{S}}^{\mathrm{T}}\mathbf{e}_1 = \int_0^L\bar{\mathbf{b}}_r\,\mathrm{d}X, \text{ on } X=0,\\
&\bar{\mathbb{S}}^{\mathrm{T}}\mathbf{e}_1 = \mathbf{0}, \text{ on } X=L.
\end{aligned} \tag{19}$$

The plate equation (17) can be integrated over X, which reduces the derivative order of the unknown variables $\{x^{(0)}(X), z^{(0)}(X)\}$. With the boundary conditions (19), the integration constants can be determined, yielding the following equation

$$\bar{S}_{11}\mathbf{e}_1 + \bar{S}_{13}\mathbf{e}_3 + \int_0^X\bar{\mathbf{b}}_r\,\mathrm{d}X - \int_0^L\bar{\mathbf{b}}_r\,\mathrm{d}X = \mathbf{0}. \tag{20}$$

This equation governs the deformation of the bottom surface of the plate, described by the unknowns $\{x^{(0)}(X), z^{(0)}(X)\}$. By substituting the expressions for the average stresses into Eq. (20), which depend on these unknowns and their derivatives, we obtain a set of ordinary differential equations (ODEs). Solving these equations allows us to determine the plate's deformed shape for given growth fields and body force distributions. Conversely, for shape-control problems, this equation serves as the theoretical basis for determining the necessary growth functions to achieve a desired target shape.

Remarks:

- While the incompressible neo-Hookean model adopted in this study captures the essential non-linear physics of large deformations, it is important to note that the formulations presented here are not restricted to this choice. For applications requiring higher fidelity across varying strain regimes, more advanced hyperelastic constitutive models can be employed. For instance, Wang et al. [71] applied the Mooney–Rivlin model within the consistent finite-strain plate theory (established through the same asymptotic series expansion method), which leads to different iterative relations for the unknowns and stresses compared to Eqs. (15) and (16). Furthermore, Yu et al. [75] incorporated a biologically motivated material model into a consistent finite-strain shell theory to investigate the inflation of arterial segments. These examples illustrate that the underlying theoretical framework is applicable to various constitutive models. The choice of the neo-Hookean model in this study serves to maintain analytical tractability, which facilitates the formulation and solution of the shape-control problems discussed in the subsequent sections.
- Although this study focuses on body forces, the developed framework can readily incorporate surface tractions on the top and bottom surfaces of the plate, such as wind or fluid pressure loads. In the process of deriving the 2D plate equation by integration through the thickness, these surface tractions are combined with the body force term to form an effective resultant force. Consequently, from the perspective of the final plate equation system, surface tractions are mathematically equivalent to an additional spatially distributed body force. Despite the need to re-derive the iterative relations of $\mathbb{S}$ and $\mathbf{x}$, this equivalence enhances the applicability of our framework to a broader range of loading scenarios.

3. Shape-control of hyperelastic plates under body forces

In this section, we present a shape-control framework for hyperelastic plates based on the derived plate equation system (Eqs. (19), (20)). The primary task is to derive explicit analytical expressions for the growth functions $\{\lambda_1^{(0)}, \lambda_1^{(1)}\}$. These functions are required to generate a prescribed target shape for a cantilever plate under specified body forces. To validate the derived formulae, we implement the growth fields in `ABAQUS` through user subroutines `UMAT` and carry out finite element simulations.

3.1. Derivation of the growth functions

Shape control is formulated as an inverse problem: given the body force distributions and boundary conditions, we seek the specific growth functions required for the plate to attain a desired target shape. Because the left end of the plate is clamped, we require that the target shape satisfies the condition ${z^{(0)}}' = 0$ at $X = 0$, i.e., no rotation at the clamp.

To derive the growth functions, we start from the integrated plate equation (20). This vector equation can be decomposed into two scalar equations along the X- and Z-directions. To eliminate derivatives of $\lambda_1^{(1)}$, we take the dot product of Eq. (20) with the tangent vector $\mathbf{r}'$, yielding the scalar condition

$$\left(\bar{S}_{11} - \int_X^L \bar{\mathbf{b}}_r \cdot \mathbf{e}_1 \, \mathrm{d}X\right) x^{(0)\prime} + \left(\bar{S}_{13} - \int_X^L \bar{\mathbf{b}}_r \cdot \mathbf{e}_3 \, \mathrm{d}X\right) z^{(0)\prime} = 0. \tag{21}$$

Substituting the expressions of the averaged stress components $\bar{S}_{11}$ and $\bar{S}_{13}$ into Eq. (21) yields an algebraic equation for the growth gradient $\lambda_1^{(1)}$:

$$\begin{aligned} &\frac{2E_r(\lambda_1^{(0)} - h\lambda_1^{(1)})}{\lambda_1^{(0)2}} - \frac{4hL_r\lambda_1^{(0)4}}{E_r{}^{5/2}} - \frac{4hL_r}{\sqrt{E_r}} - \frac{2\lambda_1^{(0)2}(3h\lambda_1^{(1)} + \lambda_1^{(0)})}{E_r} \\ &- \frac{\mathbf{b}_r^{(0)} \cdot \mathbf{r}_n h\lambda_1^{(0)}}{C_0 E_r} \\ &- \frac{x^{(0)\prime}}{C_0}\int_X^L \left(\mathbf{b}_r^{(0)} + h\mathbf{b}_r^{(1)}\right) \cdot \mathbf{e}_1 \, \mathrm{d}X - \frac{z^{(0)\prime}}{C_0}\int_X^L \left(\mathbf{b}_r^{(0)} + h\mathbf{b}_r^{(1)}\right) \cdot \mathbf{e}_3 \, \mathrm{d}X \\ &+ O(h^2) = 0. \end{aligned} \tag{22}$$

By retaining the terms of $O(1)$ and $O(h)$ in the above equation, $\lambda_1^{(1)}$ can be solved as

$$\begin{aligned} \lambda_1^{(1)} = &\frac{\lambda_1^{(0)}}{h\left(E_r{}^2 + 3\lambda_1^{(0)4}\right)} \left[E_r{}^2 - 2hL_r\sqrt{E_r}\lambda_1^{(0)} - \lambda_1^{(0)4}\left(1 + 2hL_r E_r{}^{-3/2}\lambda_1^{(0)}\right) \right. \\ &\left. - \frac{h\lambda_1^{(0)2}}{2C_0}\mathbf{b}_r^{(0)} \cdot \mathbf{r}_n - \frac{E_r\lambda_1^{(0)}}{2C_0}\mathbf{r}' \cdot \int_X^L \left(\mathbf{b}_r^{(0)} + h\mathbf{b}_r^{(1)}\right) \, \mathrm{d}X \right]. \end{aligned} \tag{23}$$

After obtaining the expression for $\lambda_1^{(1)}$, the next step is to solve for $\lambda_1^{(0)}$. However, the remaining equation is strongly nonlinear, making it difficult to solve directly by analytical methods.

To address this difficulty, we employ an asymptotic perturbation method. In many practical engineering scenarios, the magnitude of the body force is relatively small compared to the material's stiffness, which justifies the use of such a perturbation approach. Nevertheless, even when the body force is small relative to the stiffness, it can still generate significant deflections in slender plate samples. We will demonstrate these body-force-induced bending deformations across various material constants and sample thicknesses in subsequent sections (see Fig. 2). Based on the perturbation method, the body force is rewritten as $\mathbf{b}_r = (\epsilon C_0/L)\hat{\mathbf{b}}_r$, where $\hat{\mathbf{b}}_r$ is a dimensionless $O(1)$ vector field describing its spatial distribution and direction, and ϵ is a dimensionless parameter measuring the relative magnitude of the body force to the elastic stiffness. For a uniform body force in the Z-direction, we may set $\hat{\mathbf{b}}_r = \mathbf{e}_3$, giving $\epsilon = (\mathbf{b}_r \cdot \mathbf{e}_3)L/C_0$. When $|\epsilon| \ll 1$, the body force introduces only a small perturbation to a base (zero-body-force) state, so $\lambda_1^{(0)}$ differs only slightly from its base value.

Rather than adopting the undeformed configuration as the base solution, we select a stress-free grown state of broader generality. From [54], a plate subject to free growth (no external loads) can realize an arbitrary target shape in a stress-free state under the growth fields

$$\lambda_1^{(0)} = \sqrt{E_r}, \quad \lambda_1^{(1)} = -\frac{L_r}{\sqrt{E_r}}. \tag{24}$$

In the absence of body forces, the growth functions in Eq. (24) give $\mathbb{S}^{(0)} = \mathbb{S}^{(1)} = \mathbf{0}$. The current configuration is thus an equilibrium of minimal elastic energy. Using this stress-free configuration as the base state is advantageous because it is stable and can accommodate a broad scope of target shapes. Furthermore, its stability and flexibility are crucial for practical engineering applications in soft materials. Hence, we assume that the growth fields take the form

$$\begin{aligned} \lambda_1^{(0)} = &\sqrt{E_r}(1 + \epsilon f), \\ \lambda_1^{(1)} = &-\frac{L_r}{\sqrt{E_r}} - \frac{\epsilon}{8\sqrt{E_r}hL}\left[8Lf\left(E_r + hL_r\right) \right. \\ &\left. + h\hat{\mathbf{b}}_r^{(0)} \cdot \mathbf{r}_n + \sqrt{E_r}\mathbf{r}' \cdot \int_X^L \left(\hat{\mathbf{b}}_r^{(0)} + h\hat{\mathbf{b}}_r^{(1)}\right) \mathrm{d}X \right], \end{aligned} \tag{25}$$

where f is an unknown function to be determined, and the expression for $\lambda_1^{(1)}$ here has been updated by collecting the $O(1)$ and $O(\epsilon)$ terms from Eq. (23). In the absence of body forces (i.e., $\epsilon = 0$), Eq. (25) reduces to the stress-free solution given by Eq. (24).

The final step is to solve for f. Substituting the perturbation form (25) into Eq. (20) and retaining terms of order $O(\epsilon)$ yields two equations. These scalar equations correspond to the X and Z directions and both involve f, f', and f''. Solving the first equation for f'' and substituting into the second gives an explicit expression for f'

$$\begin{aligned} f' = &\frac{1}{8hL(E_r + 6hL_r)}\left[E_r\mathbf{r}_n \cdot \int_X^L \left(3\hat{\mathbf{b}}_r^{(0)} + 3h\hat{\mathbf{b}}_r^{(1)} + 2h^2\hat{\mathbf{b}}_r^{(2)}\right) \mathrm{d}X \right. \\ &\left. + 2hL_r\mathbf{r}_n \cdot \int_X^L \left(\hat{\mathbf{b}}_r^{(0)} + h\hat{\mathbf{b}}_r^{(1)}\right) \mathrm{d}X \right] + \frac{1}{8L\sqrt{E_r}}\hat{\mathbf{b}}_r^{(0)} \cdot \mathbf{r}'. \end{aligned} \tag{26}$$

Integrating f' with respect to X gives the analytical expression of f, with the integration constant determined by the boundary condition $f(L) = 0$ (free end at $X = L$). The explicit expression for f is not presented here due to the complexity of the integration in the general case. Instead, for target shapes with complicated parametric equations, a numerical integration approach is recommended. By substituting the determined f into Eq. (25), we obtain the asymptotic solutions for $\lambda_1^{(0)}$ and $\lambda_1^{(1)}$ that incorporate body-force effects. It is important to note that while the $O(\epsilon)$ correction to $\lambda_1^{(0)}$ is generally modest, the correction to the gradient term $\lambda_1^{(1)}$ can be substantial, particularly for slender, compliant plates.

As discussed in the Remarks of Section 2, the theoretical framework established here is generic. For other incompressible hyperelastic models (e.g., Mooney–Rivlin or Gent), the iterative relations for the unknowns $\mathbf{x}^{(n)}$ and pressure $p^{(n)}$ can be derived following the same asymptotic expansion procedure. Consequently, the solution strategy for the inverse problem remains applicable by defining the perturbation parameter ϵ through the equivalent initial shear modulus. Although the asymptotic solutions (25) retain only first-order terms in ϵ, numerical results in Sections 3.3 and 3.4 show that they perform well even under significant body-force loading. Before proceeding to the representative examples, we propose a shape-control framework based on the derived growth functions.

Remark: We acknowledge that in classic beam theory, the dimensionless parameter governing the effective bending under gravity is $\epsilon L^2/h^2$. However, we maintain ϵ as the independent perturbation parameter for the following reasons. First, the validity of the perturbation method relies on the expansion parameter being small ($\ll$1). The parameter $\epsilon L^2/h^2$ can reach order $O(1)$ or larger for slender, soft structures (the "heavy elastica" regime), making it unsuitable for use as a small perturbation parameter. In contrast, our defined ϵ remains consistently small for the materials considered. Second, introducing h into the definition of ϵ would couple the geometric scale h and the loading scale ϵ, complicating the separation of orders in the governing equations. Keeping ϵ independent of h allows us to systematically solve for the $O(1)$ and $O(\epsilon)$ terms at each order of h. Third, simple parameter rescaling using $\epsilon L^2/h^2$ is insufficient to capture the full nonlinear response. Verification confirms that plates with different thicknesses but identical $\epsilon L^2/h^2$ do not exhibit identical dimensionless deflection profiles (one can compare the results from Fig. 2), indicating that geometric nonlinearity couples with thickness h in a complex manner. This confirms that treating ϵ and h as independent parameters is physically necessary.

3.2. The shape-control framework

This subsection summarizes a practical workflow to compute growth fields that program a cantilever plate into a target shape under prescribed body forces, based on the asymptotic solutions (25)–(26).

First, we clarify the modelling setting and assumptions. We consider a plane-strain, incompressible neo-Hookean plate with material constant C_0 in a cantilever configuration: clamped at $X = 0$, free at $X = L$, and traction-free on the top and bottom faces. The growth tensor is diagonal and varies linearly through the thickness, $\lambda_1(X, Z) = \lambda_1^{(0)}(X) + Z\lambda_1^{(1)}(X)$, where $\lambda_1^{(0)}$ and $\lambda_1^{(1)}$ depend only on X. A small parameter $|\epsilon| \ll 1$ is introduced to represent the effect of body forces $\mathbf{b}_r = (\epsilon C_0/L)\hat{\mathbf{b}}_r$.

With the explicit asymptotic formulae for the growth functions derived above, we outline a step-by-step framework that incorporates analytical calculations of $\lambda_1^{(0)}(X)$ and $\lambda_1^{(1)}(X)$ with numerical verification:

1. Specify geometry, material constants, and body force. Set values for L, h (total thickness $2h$), and W (only L and h enter the plate model), and the material constant C_0. Prescribe the body force $\mathbf{b}_r(X, Z)$ and its Taylor expansion coefficients $\{\mathbf{b}_r^{(0)}(X), \mathbf{b}_r^{(1)}(X), \mathbf{b}_r^{(2)}(X)\}$.
2. Define the target shape of the bottom face. Provide the parametric equation of the bottom face $\mathbf{r}(X) = (x^{(0)}(X), z^{(0)}(X))$ on $X \in [0, L]$. To ensure compatibility at the clamped end $X = 0$, the tangent of $\mathbf{r}$ should match the orientation of the clamp. For example, we have $z^{(0)\prime}\big|_{X=0} = 0$ corresponding to a horizontal clamp.
3. Calculate the growth functions. Evaluate geometric quantities E_r and L_r of $\mathbf{r}(X)$ according to (14). Compute $f'(X)$ from (26), then integrate $f'(X)$ over X with the boundary condition $f(L) = 0$ (free end) to obtain $f(X)$. When an analytical explicit expression of $f(X)$ is unavailable, one can adopt a numerical method for integration. Substitute $f(X)$ into Eq. (25) to obtain the required growth functions $\lambda_1^{(0)}$ and $\lambda_1^{(1)}$ that generate the target shape under the given body forces.
4. Numerical verification. Implement the growth functions in a 3D FE model (e.g., ABAQUS through a hyperelastic UMAT that realizes $\mathbb{F} = \mathbb{A}\mathbb{G}$). In the FE model, the growth functions are input as state variables. These state variables are updated incrementally during the simulation: at each time step t, the growth tensor is interpolated as $\mathbb{G}(t) = (1 - t)\,\mathbb{I} + t\,\mathbb{G}$, such that the growth tensor varies linearly from $\mathbb{I}$ (initial state) to the target $\mathbb{G}$ (fully grown) over the simulation. This ensures a smooth transition from the reference configuration to the grown state. Finally, compare the simulated profile of the plate with the target shape.

It is well known that the sequence of applying growth and external loads plays a critical role in the behaviour of nonlinear morphing systems, particularly for slender or compliant plates where multiple equilibrium branches and snap-through instabilities may exist [76]. In practice, by adjusting the evolution of the applied loads and growth fields, one can steer the system towards the desired equilibrium branch and avoid unintended snap-through. To address this, we consider three basic paths: (i) apply the body force first and then growth; (ii) apply growth first and then the body force; and (iii) apply body force and growth simultaneously. A detailed sensitivity analysis comparing these paths is provided in Appendix A, which reveals that the final equilibrium shape is dependent on the loading sequence, especially for thin plates under large body forces. For thick or stiff plates, the difference under these paths is usually negligible, but for thin/soft plates, the two-stage path proposed below is typically more robust, especially when the influence of body force is not small (i.e., $|\epsilon| \ll 1$ does not hold). Path-i and path-iii are more sensitive and prone to premature buckling when programming against body force. Motivated by these observations, we propose a two-stage loading strategy (i.e., path-iv) that begins from the stress-free grown shape and then applies both the body forces and the correction of growth fields:

- Stage I (growth-only to the stress-free state): apply the growth tensor from the identity to the stress-free growth $\mathbb{G}_0 = \mathbb{G}\big|_{\epsilon=0}$ that realizes the target shape in the absence of body forces (i.e., $\mathbf{b}_r = \mathbf{0}$). Actually, the growth functions related to the stress-free state are given by (24). During the step time $t_1 \in [0, 1]$, we have $\mathbb{G} = (1 - t_1)\mathbb{I} + t_1\mathbb{G}_0$. This stage brings the plate to the stress-free target shape (without body forces), suppressing body force-triggered compression/buckling so that Stage II starts from a stable, low-stress base state.
- Stage II (simultaneous application of body force and correction of growth field): starting from the stress-free state $\mathbb{G}_0$, increase both the body force and the $O(\epsilon)$ correction in the growth field linearly with step time $t_2 \in [0, 1]$ until the growth tensor reaches the final design $\mathbb{G}_1$. At the end of this stage, the growth functions $\lambda_1^{(0)}$ and $\lambda_1^{(1)}$ are given by Eq. (25) evaluated at the prescribed ϵ. During this stage, we have

$$\mathbf{b}_r(t_2) = t_2\,\mathbf{b}_r, \quad \mathbb{G} = (1 - t_2)\mathbb{G}_0 + t_2\mathbb{G}_1.$$

  With this loading path, the final configuration settles near the intended target shape.

As demonstrated in Appendix A (see Fig. A.1), this strategy is relatively robust compared to other loading sequences, avoiding premature buckling or chaotic intermediate states. If noticeable mismatch or instability persists, one can further fine-tune the loading path by adjusting the relative rates of the applied body forces and growth fields. In the following content, we present a series of examples to demonstrate the accuracy and efficiency of the proposed theoretical framework for shape control.

3.3. Examples under uniform body forces

Uniform body forces represent a canonical loading scenario in engineering applications, such as the gravitational force acting on a plate. In this subsection, we demonstrate shape programming for a cantilever plate subjected to a uniform body force (e.g., gravity).

We first investigate the forward problem of plate deformation under pure gravitational loading (i.e., without growth). Geometric and material parameters, specifically plate thickness and shear modulus, significantly influence the bending deflection. Larger deflections impose greater challenges for shape control through growth-induced deformation. To assess the impact of different parameter combinations on the plate's deformation, we maintain a constant body force while varying the thickness and shear modulus.

The numerical simulations are performed in ABAQUS/Standard using a 3D geometric model. To enforce the plane-strain assumption, we apply displacement constraints ($U_Y = 0$) on the whole model. The domain is discretized using 20-node quadratic hybrid brick elements (C3D20H), which are specifically chosen to prevent volumetric locking in incompressible hyperelastic materials. To ensure accuracy and mesh-independence, a mesh sensitivity analysis is conducted and a refined mesh density along the longitudinal and thickness directions is adopted, yielding converged solutions for the deflection profiles (see Appendix B). The clamped boundary condition at $X = 0$ is implemented by constraining all translational degrees of freedom, ensuring an alignment between the computational setup and the theoretical assumptions.

The numerical simulation results are presented in Fig. 2 (solid lines represent the bottom profiles of the plates). In these simulations, the plate is initially straight and clamped at the left end, with a length of $L = 1$ m and various thicknesses $2h = \{0.01, 0.02, 0.05, 0.1\}$ m. The material density is set to $\rho_r = 1000\ \mathrm{kg/m^3}$, and the force per unit mass is $\mathbf{g} = -10\mathbf{e}_3\ \mathrm{N/kg}$, resulting in a constant body force

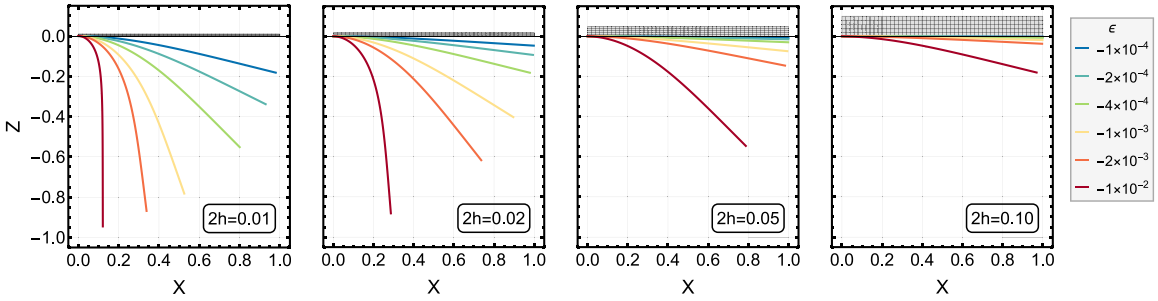


Fig. 2. Forward problem of gravity-induced bending in a cantilever plate without growth. The plots show the deformed bottom profiles (solid lines) for plates with varying thicknesses $2h$. The colour gradient from blue to red indicates increasing magnitude of the dimensionless body force parameter ϵ.

distribution of $\mathbf{b} = \rho_r \mathbf{g} = -10^4 \mathbf{e}_3$ N/m^3. We vary the material constant $C_0 = \{100, 50, 25, 10, 5, 1\}$ MPa to adjust the value of the dimensionless parameter ϵ. By setting $\hat{\mathbf{b}}_r = \mathbf{e}_3$, the dimensionless parameter ϵ can be expressed as $\epsilon = \mathbf{b}_r \cdot \mathbf{e}_3 L/C_0 = -10^4 L/C_0$. Results for different values of $\epsilon = -\{0.01, 0.02, 0.04, 0.1, 0.2, 1\} \times 10^{-2}$ are represented by colours transitioning from blue to red.

It is observed that even when the parameter $|\epsilon|$ is as small as 0.01, it still has a significant impact on the deflections of thin plates. Our numerical results demonstrate that as either thickness or shear modulus increases, the plate's deflection decreases, thereby enhancing its resistance to gravitational loading. Fig. 2 provides a baseline map of gravity-induced deflection for the initial (no-growth) cantilever plate across a range of thicknesses and ϵ values. In the following shape-control examples, each result can be directly compared against its corresponding gravity-only case in Fig. 2 to assess how much deflection is counteracted.

To verify the shape-control framework, we begin with illustrative examples corresponding to target shapes with zero and constant curvatures.

• Examples of flat shape

The first example addresses a common engineering scenario: maintaining a flat, horizontal plate under gravity. This case is critical in numerous applications where flatness is essential, such as in precision manufacturing and large-scale architectural components like flat roofs or floors, which tend to sag under their own weight. Our method calculates the required growth fields to counteract gravitational deformation and restore the initial flat configuration. In this case, the target shape is defined as $x^{(0)} = X$ and $z^{(0)} = 0$, and its geometric fundamental quantities are $E_r = 1$ and $L_r = 0$. By substituting $x^{(0)}$ and $z^{(0)}$ into Eq. (26), we obtain $f' = 3(L-X)/(8hL)$. Integrating $f'(X)$ with respect to X and enforcing the boundary condition $f(L) = 0$ yields

$$f = -\frac{3(L-X)^2}{16hL}. \tag{27}$$

Substituting $f(X)$ into the perturbation solution (25), we compute the growth fields required to achieve the target shape:

$$\begin{aligned} &\text{Target shape:} \quad x^{(0)} = X, \quad z^{(0)} = 0, \\ &\text{Growth functions:} \quad \lambda_1^{(0)} = 1 + \epsilon f, \quad \lambda_1^{(1)} = -\frac{\epsilon(8Lf + h)}{8hL}. \end{aligned} \tag{28}$$

To validate the derived growth functions presented in Eq. (28), we developed a user-defined material subroutine UMAT and conducted numerical simulations. The simulation setup incorporates various plate thicknesses $2h$ and ϵ, consistent with those illustrated in Fig. 2. For most cases, the loading path applies the body force first, followed by the growth field. For thin and compliant plates, the two-stage strategy introduced in Section 3.2 is adopted. In the first stage, the growth field is prescribed with $\epsilon = 0$ to reach the stress-free target shape in the absence of body force. The second stage involves applying the body force and the $O(\epsilon)$ growth correction simultaneously.

The numerical results are compared with the target shape in Fig. 3(a). The figure shows that for most cases, the simulated shapes align closely with the target shape, demonstrating that the proposed growth field effectively compensates for gravity-induced deformations. Nevertheless, a noticeable deviation is observed for a particularly thin plate under significant gravitational effects ($2h = 0.01$ and $\epsilon = -0.01$), suggesting that the growth field design may require further optimization under such extreme conditions.

To visualize the entire deforming process, we implement a gravity-first loading sequence in the finite element analysis. As shown for selected cases ($2h = 0.02$ and 0.05, with $\epsilon = -0.01$) in Fig. 3(b), the plate initially bends under gravity and subsequently recovers its flat configuration through the applied growth field. The contour plot in Fig. 3(b) illustrates the magnitude of $\mathrm{Det}\,\mathbb{G}$. It reveals that the growth field is highly non-uniform, particularly near the clamped end. To counteract gravitational bending, the upper portion of the plate undergoes contraction ($\mathrm{Det}\,\mathbb{G} < 1$), while the lower portion experiences expansion ($\mathrm{Det}\,\mathbb{G} > 1$). As the plate becomes thinner, the gradient of $\mathrm{Det}\,\mathbb{G}$ increases.

• Examples of semicircle shapes

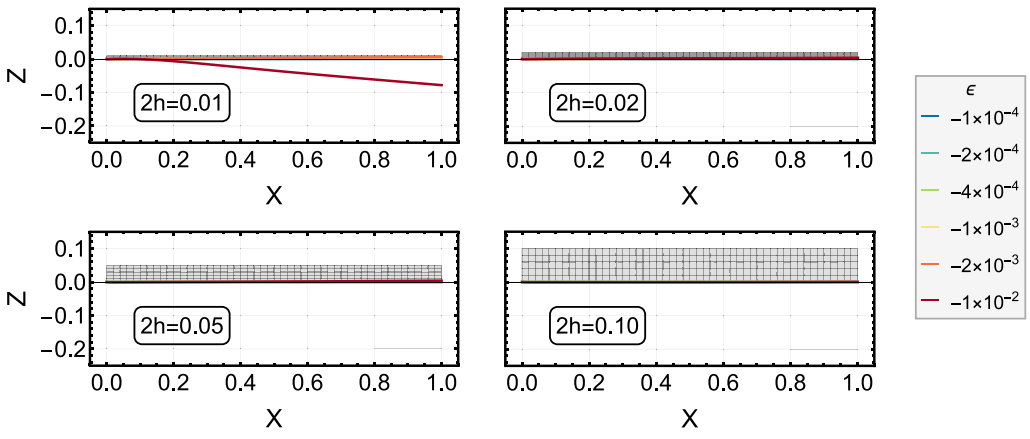
Next, we explore two examples with constant, non-zero curvature to validate the method's capability to achieve more complex shapes. We prescribe an upward-bending semicircle ($L_r > 0$) and a downward-bending semicircle ($L_r < 0$) as the target shapes. Following the procedure in the previous examples, we first define the parametric equations for the semicircle shapes (with diameter 1) as $x^{(0)} = 1/2\sin(\pi X)$ and $z^{(0)} = \pm 1/2[\cos(\pi X) - 1]$. The corresponding geometric fundamental quantities are $E_r = \pi^2/4$ and $L_r = \pm\pi^2/2$. By substituting $x^{(0)}$ and $z^{(0)}$ into Eq. (26), we obtain the expression for f'. Integrating $f'(X)$ with respect to X and applying the boundary condition $f(L) = 0$ to determine the integration constant, we obtain

$$\begin{aligned} f = &\frac{1}{16\pi h(12h\,\mathrm{Sign}(L_r) + 1)L} \Big[3\left(8h^2 + 2h\,\mathrm{Sign}(L_r) + 1\right) \\ &\times (\cos(\pi L) - \cos(\pi X)) \\ &+ \pi(4h\,\mathrm{Sign}(L_r) + 3)(L - X)\sin(\pi X) \Big], \end{aligned} \tag{29}$$

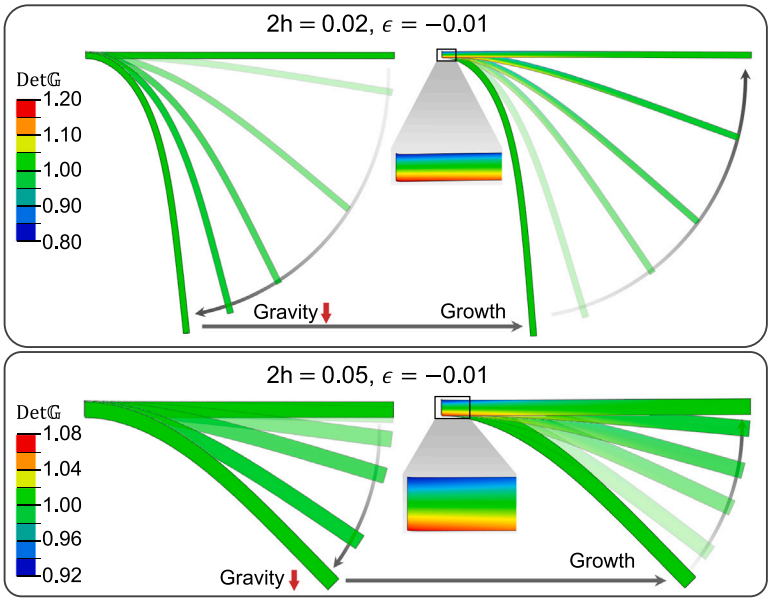
where $\mathrm{Sign}(L_r)$ is the sign function of L_r. Substituting $f(X)$ into the perturbation solution (25), we compute the growth fields required to achieve the target shapes:

$$\begin{aligned} &\text{Target shapes:} \quad x^{(0)} = \frac{1}{2}\sin(\pi X), \quad z^{(0)} = \pm\frac{1}{2}\left[\cos(\pi X) - 1\right], \\ &\text{Growth functions:} \quad \lambda_1^{(0)} = \frac{1}{2}\pi(1 + \epsilon f), \\ &\qquad \lambda_1^{(1)} = \frac{-\,\mathrm{Sign}(L_r)}{16hL} \Big[16\pi hL + \pi\epsilon(L - X)\sin(\pi X) \\ &\qquad\qquad + 8\pi(2h + \mathrm{Sign}(L_r))L\epsilon f + 2h\epsilon\,\mathrm{Sign}(L_r)\cos(\pi X) \Big]. \end{aligned} \tag{30}$$

To verify the derived growth functions in Eq. (30), we conducted numerical simulations. Similar to previous examples, for most cases,



(a)



(b)

Fig. 3. Shape control for a flat target configuration under gravity. (a) Comparison between the target horizontal shape (blue line) and simulated bottom profiles (solid curves) for various thicknesses $2h$ and body force parameters ϵ. (b) Visualization of the deformation process and the determinant of the growth tensor $\mathrm{Det}\,\mathbb{G}$ for selected cases ($2h = 0.02, 0.05$; $\epsilon = -0.01$).

the body force is applied first, followed by growth. For thin compliant plates, the two-stage loading path introduced in Section 3.2 is used. As shown in Fig. 4(a) and (b), the simulated profiles closely match the target shape, demonstrating the effectiveness of our method in compensating for gravity-induced deformations. However, there are notable differences between the upward and downward bending cases, particularly under conditions of small modulus and strong gravitational loading.

- For the downward-bending semicircle, where the curvature aligns with the direction of gravity, our simulated results yield good agreement with the target shape across all tested parameters. In this scenario, the body force acts in an assisting role, helping the plate achieve and maintain the desired configuration.
- For the upward-bending semicircle, where the plate is programmed to bend against gravity, the body force introduces a destabilizing effect. This is pronounced for the thin plate ($2h = 0.01$) under strong gravitational effects ($\epsilon = -0.01$). In this extreme case, the plate fails to attain the target shape and collapses into a self-intersecting configuration.

The collapse observed in Fig. 4(a) signifies a structural instability, specifically a snap-through buckling phenomenon triggered when the target shape opposes the gravitational field [76,77]. Detailed discussion on the physical mechanism of this instability and the threshold is provided in Section 5.

We observe that the upward- and downward-bending semicircular plates exhibit noticeably different distributions of $\mathrm{Det}\,\mathbb{G}$. A representative case (with $2h = 0.05$ and $\epsilon = -0.01$) is chosen to illustrate the contour plot of $\mathrm{Det}\,\mathbb{G}$ in Fig. 5. Since the target geometry is prescribed for the bottom surface of the plate, the outer arc of the downward-bending plate is slightly longer than that of the upward-bending plate (with the difference corresponding to the thickness $2h$). Therefore, the downward-bending case requires a slightly larger overall

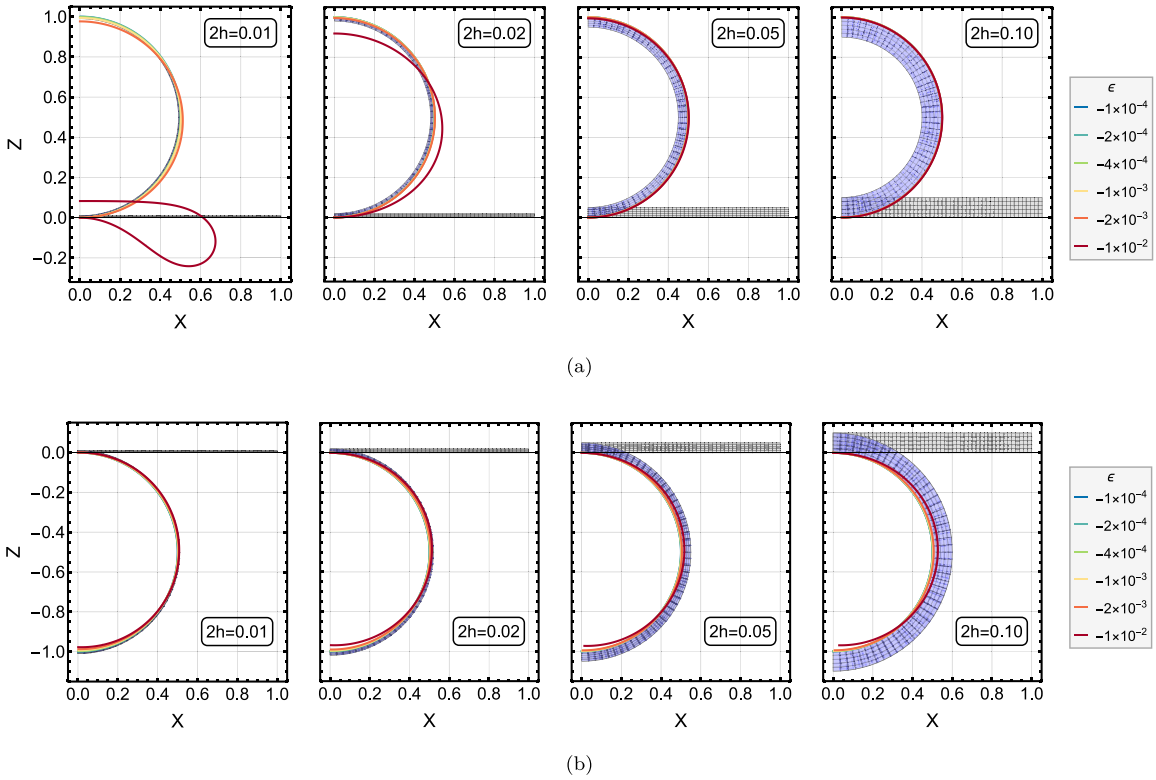


Fig. 4. Shape control for semicircular target shapes. The plots compare the target geometry (blue curves) with simulated bottom profiles (solid lines) across different thicknesses $2h$ and body force parameters ϵ. (a) Upward-bending semicircle ($L_r > 0$). (b) Downward-bending semicircle ($L_r < 0$).

Det $\mathbb{G}$. Specifically, when the target shape (upward-bending) opposes the natural deformation trend induced by gravity, the growth field on the left end of the plate provides a large gradient through the thickness to generate a sufficient bending moment to counteract the gravitational load. Conversely, when the target shape (downward-bending) aligns with the gravity-induced bending mode, the body force actually assists shape control, and thus the required growth gradient is considerably smaller.

It is worth noting that the deflections shown in Fig. 2 also represent the shape error that would occur if classical stress-free inverse design methods (e.g., [54]) were applied in a gravity-dominant environment. In contrast to the significant deflections observed in the baseline cases (Fig. 2), the proposed method (Fig. 3) effectively eliminates the gravity-induced deviations. This observation reveals a design principle: strategically harnessing rather than opposing external body forces such as gravity can markedly reduce the gradient of the required growth field. Detailed discussion on this principle is provided in Section 5.

3.4. Examples under spatially inhomogeneous body forces

In this subsection, we extend the shape-control framework to plates under spatially inhomogeneous body forces. Specifically, we consider a linearly varying body force, a scenario frequently encountered in engineering applications. Such loading can represent the self-weight of a tapered structure or a first-order approximation of a more complex load profile.

To establish a baseline for shape control, we first analyse the plate's deflection under the linear load (without growth). Similar to Section 3.3, we investigate the body-force-induced deflections by simulating the deformation for various thicknesses and shear moduli under a fixed load distribution.

The numerical results are shown in Fig. 6, where solid curves denote the deformed bottom profiles. The plate's geometric parameters are identical to those adopted in Section 3.3. The material density is set to $\rho_r = 500(1 + X)$ kg/m^3, and the force per unit mass is $\mathbf{g} = -10\mathbf{e}_3$ N/kg, resulting in a linear body force distribution of $\mathbf{b} = \rho_r\mathbf{g} = -5000(1+X)\mathbf{e}_3$ N/m^3. The material constant takes different values $C_0 = \{100, 50, 25, 10, 5, 1\}$ MPa to adjust the value of the dimensionless parameter ϵ. By setting $\hat{\mathbf{b}}_r = 0.5(1+X)\mathbf{e}_3$, the dimensionless parameter ϵ can be expressed as $\epsilon = L/C_0 = -10^4 L/C_0$. Numerical implementation details (element type, boundary conditions, and solution procedures) follow those in Section 3.3. Although the deflection profiles shown in Fig. 6 appear qualitatively similar to those under uniform loading (Fig. 2), it should be noted that they result from a linearly distributed body force.

• Examples of parabolic shapes

In this example, we aim to achieve a parabolic target shape, a common geometric profile in engineering for applications such as reflective surfaces for antennas or solar concentrators. The target shapes are selected as parabolas bending upwards ($L_r > 0$) and downwards ($L_r < 0$). In this case, the parametric equations are defined as $x^{(0)} = X$ and $z^{(0)} = \pm 1/2X^2$, and its geometric fundamental quantities are $E_r = 1 + X^2$ and $L_r = \pm 1/\sqrt{(1 + X^2)}$. By substituting $x^{(0)}$ and $z^{(0)}$ into Eq. (26), we obtain the derivative of f as follows

$$f' = \frac{1}{32\sqrt{a}hL\left(a^{3/2} + 6h\,\mathrm{Sign}(L_r)\right)}\Big[\,3a^2\left(-a + (L+1)^2 - 2X\right) + 12h^2(a + X - 1) + 2\sqrt{a}h\,\mathrm{Sign}(L_r)\left(L(L+2) + X^4 + X^3 - X\right)\Big], \tag{31}$$

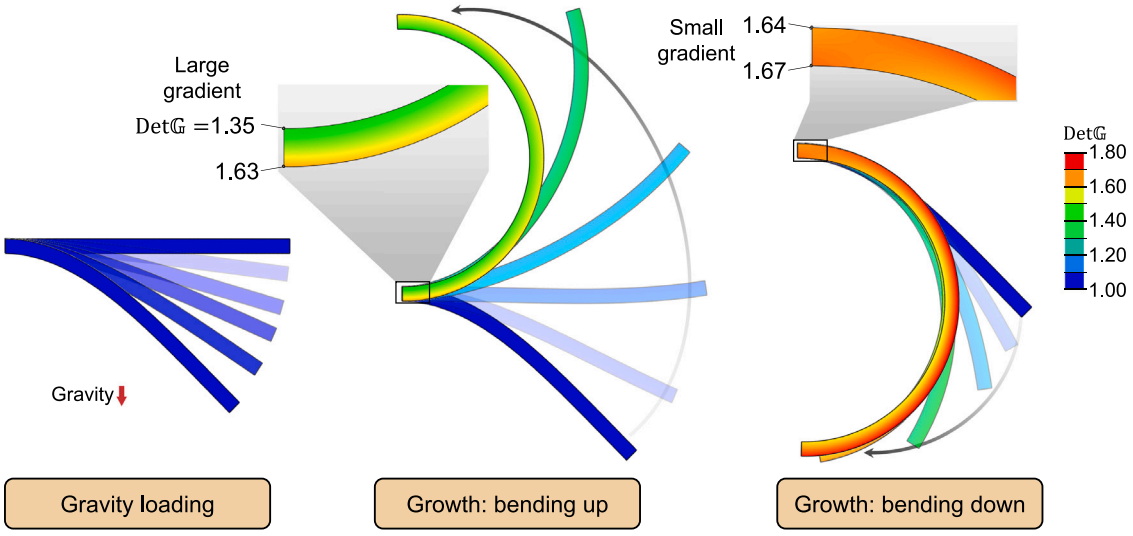


Fig. 5. Comparison of the required growth fields for upward- and downward-bending semicircles ($2h = 0.05$, $\epsilon = -0.01$). The contour plots display $\mathrm{Det}\,\mathbb{G}$ during the deformation. The upward-bending case (left) requires a significantly larger growth gradient through the thickness to oppose gravity, whereas the downward-bending case (right) utilizes gravity to assist deformation, requiring a milder growth gradient.

where the quantity $a = 1 + X^2$. Since the integration of $f'(X)$ with respect to X is complex, we use numerical methods to compute $f(X)$ by prescribing the geometric parameters h and L and applying the boundary condition $f(L) = 0$ to determine the integration constant. Substituting $f(X)$ into the perturbation solution (25), we obtain the growth fields required to achieve the target shape:

$$\begin{aligned}
&\text{Target shapes:} \quad x^{(0)} = X, \quad z^{(0)} = \pm\frac{1}{2}X^2,\\
&\text{Growth functions:} \quad \lambda_1^{(0)} = \sqrt{a}(1+\epsilon f),\\
&\qquad \lambda_1^{(1)} = \frac{\mathrm{Sign}(L_r)}{32ahL}\Big[-32L\left(h+\epsilon f\left(\mathrm{Sign}(L_r)a^{3/2}+h\right)\right)\\
&\qquad\quad + a\epsilon\left(a(X+2)-X(L+1)^2-2\right)\\
&\qquad\quad - 2\epsilon\,\mathrm{Sign}(L_r)\sqrt{a}h(X+1)\Big].
\end{aligned} \tag{32}$$

To validate the derived growth functions presented in Eq. (32), we conducted numerical simulations. The simulation setup incorporates various plate thicknesses $2h$ and ϵ, consistent with those illustrated in Fig. 6. The resulting configurations are compared against the target shapes, as depicted in Fig. 7(a). It shows that the numerically obtained profiles align closely with the target shapes. These results demonstrate that our shape-control framework remains robust and effective for controlling the plate's configuration even under non-uniform body force distributions.

• Examples of spiral shapes

In this example, we program a spiral target shape representative of plant tendrils and other natural coils. This form is common in nature, from plant tendrils to animal horns, making it a typical reference for biomimetic design. Researchers have designed biomimetic grippers that utilize differential growth to achieve grasping and releasing functions [78–81]. We demonstrate through this example that our growth-based shape-control framework can generate similar shapes.

In this case, the parametric equation and geometric fundamental quantities of the target shape are defined as

$$\begin{aligned}
&x^{(0)} = \frac{3}{5}X\cos\left(2\pi X^2\right), \quad z^{(0)} = \frac{3}{5}X\sin\left(2\pi X^2\right),\\
&E_r = \frac{9}{25}b, \quad L_r = \frac{12\pi X(b+2)}{5\sqrt{b}},
\end{aligned} \tag{33}$$

where the quantity $b = 16\pi^2X^4 + 1$. With the prescribed $x^{(0)}$ and $z^{(0)}$ (33), we obtain the derivative of f from Eq. (26) as follows

$$\begin{aligned}
f' = &\frac{-1}{160bhL\left(b^{3/2}+40\pi(b+2)hX\right)}\Big[\cos\left(2\pi X^2\right)\\
&\times\Big(-9b^{5/2}(L-X)(L+X+2)\\
&-100\sqrt{b}(b+2)h^2\left(b+16\pi^2X^3-1\right)-40\pi bhX\left((b+2)L(L+2)\right.\\
&\left.-(b+4)X-2X^2\right)\Big)\\
&-2\sin\left(2\pi X^2\right)\Big(18\pi b^{5/2}X^2(X-L)(L+X+2)\\
&+200\pi(b+2)\sqrt{b}h^2X(X+1)\\
&+5bh\left(-16\pi^2(b+2)L(L+2)X^3+b(b+2)X+b(2b+3)\right.\\
&\left.-2(X+2)\right)\Big)\Big].
\end{aligned} \tag{34}$$

$f'(X)$ is numerically integrated over X, with the integration constant determined by the boundary condition $f(L) = 0$. Substituting $f(X)$ into the perturbation solution (25), we compute the required growth fields

$$\begin{aligned}
&\lambda_1^{(0)} = \frac{3}{5}\sqrt{b}(1+\epsilon f),\\
&\lambda_1^{(1)} = \frac{1}{640b}\Big[-\frac{128\epsilon f}{h}\left(3b^{3/2}+20\pi(b+2)hX\right)-2560\pi(b+2)X\\
&\quad+\frac{\sqrt{b}\epsilon}{\pi hL}\Big(4\pi\sin\left(2\pi X^2\right)\left(40\pi hX^2(X+1)\right.\\
&\quad\left.-3\sqrt{b}(L-X)(L+X+2)\right)\\
&\quad+\cos\left(2\pi X^2\right)\left(3\sqrt{b}\left(b-16\pi^2X^2(L(L+2)-2X)-1\right)\right.\\
&\quad\left.-40\pi h(X+1)\right)\Big)\Big].
\end{aligned} \tag{35}$$

To validate the derived growth functions in Eq. (35), we conducted numerical simulations. The simulation setup is consistent with that illustrated in Fig. 6. The resulting configurations are compared with the target shape, as depicted in Fig. 8(a). Fig. 8(b) shows the distributions of $\mathrm{Det}\,\mathbb{G}$ for two representative cases during deformation. The growth and body forces are applied simultaneously for better visualization

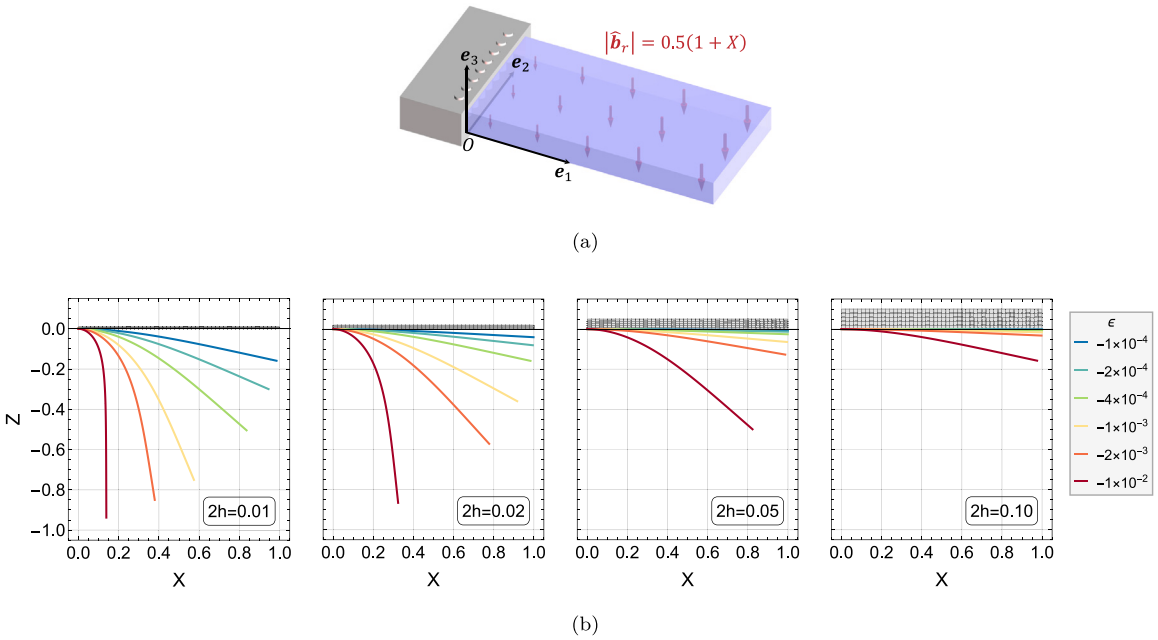


Fig. 6. Forward problem under linearly distributed body forces. (a) Illustration of the linearly distributed body force $\hat{\mathbf{b}}_r = 0.5(1+X)\mathbf{e}_3$. (b) Gravity-induced bending profiles (without growth) for various thicknesses $2h$ and dimensionless load parameters ϵ.

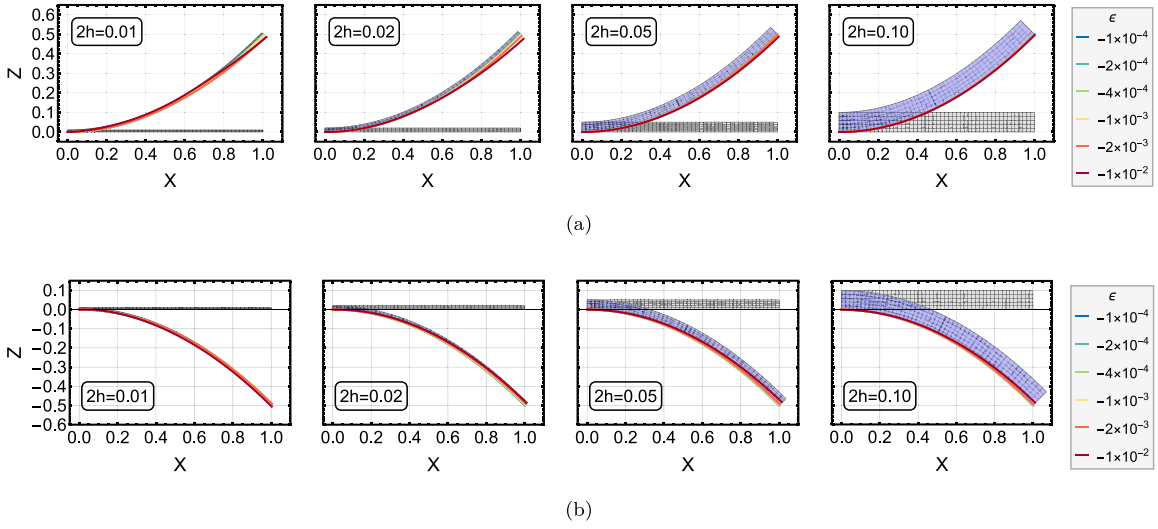


Fig. 7. Shape control for parabolic target shapes under linearly distributed body forces. (a) Upward-bending parabola ($z^{(0)} = 0.5X^2$). (b) Downward-bending parabola ($z^{(0)} = -0.5X^2$).

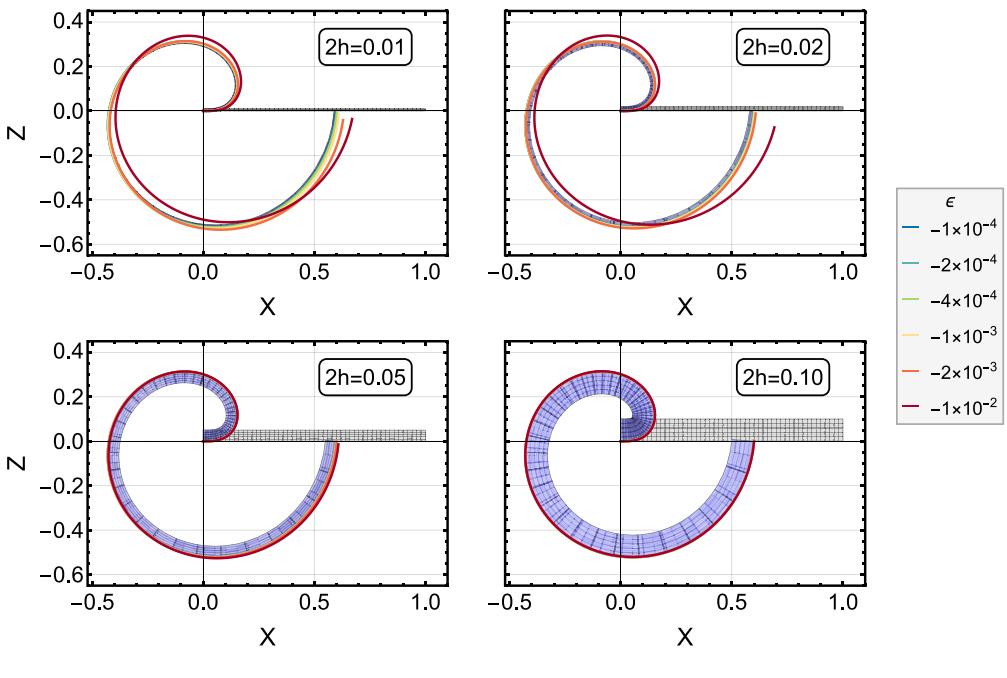
(this single-step loading path yields the same final equilibrium as the two-stage path used in other examples). It shows that the numerically obtained shapes align closely with the target shapes in most cases.

To define the operational limits of our framework, we performed a systematic error analysis across the design space, as shown in Fig. 9. We quantify the deviation using the root-mean-square error, defined as

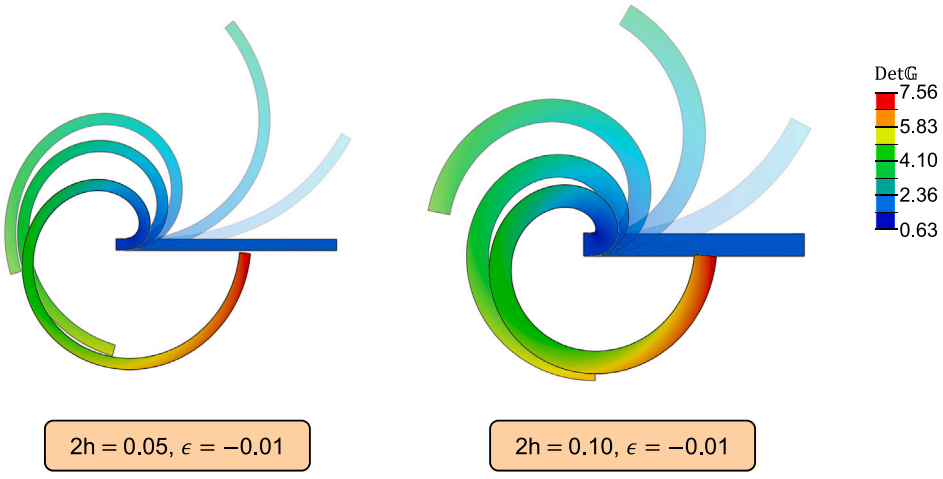
$$\text{Error} = \sqrt{\frac{1}{L}\int_0^L \|\mathbf{r}(X) - \mathbf{r}_{\text{target}}(X)\|^2 \, \mathrm{d}X}, \tag{36}$$

where $X \in [0, L]$ and $\|\cdot\|$ denotes the norm. As illustrated in Fig. 9, the error remains negligible (typically below 0.01) for the majority of the design space, indicating the robustness of our method. High-error regions are observed primarily in the regime of large body forces ($\epsilon \to -0.01$) and small thickness ($2h/L \to 0.01$). In the upward-bending semicircle case, the significant deviations are primarily attributed to structural instabilities, such as snap-through buckling, which prevent the structure from attaining the target configuration. Furthermore, this case corresponds to extreme parameter regimes characterized by dominant gravitational effects. Excluding this instability case, the errors for all other target shapes remain consistently low (below 0.05) even within these extreme parameter ranges, demonstrating the general applicability of our framework.

In this section, we have presented and validated the shape-control framework for achieving various target geometries under both uniform and spatially inhomogeneous body forces. Through a series of examples including flat, semicircular, parabolic, and spiral shapes, we have demonstrated that the simulated results generally show good



(a)



(b)

Fig. 8. Shape control for a spiral target shape under linearly distributed body forces. (a) Comparison of the target spiral profile (blue) and simulated shapes (solid lines). (b) Evolution of the deformation and Det $\mathbb{G}$ distribution for plates with thicknesses $2h = 0.05$ and 0.1 ($\epsilon = -0.01$).

agreement with the predefined target shapes. This confirms the effectiveness of our derived asymptotic analytical formulae and the two-stage loading strategy. In structural engineering, an analogous shape control approach in small strain regimes underlies pre-tensioning of reinforcing steel in concrete to introduce beneficial compressive residual stresses [82]. These residual stresses can mitigate gravity- or service-load induced small deflections. In contrast, the present finite-strain shape-control framework broadens the applicability scope to nonlinear regimes, enabling the control of slender compliant structures undergoing large deformations.

4. Experimental validation

Having validated the asymptotic analytical solutions against finite element simulations for general loading cases in Section 3, we proceed to experimental validation. This section bridges theoretical derivation with physical implementation by utilizing the growth functions derived in Eq. (25) as the governing inputs for inverse design. We aim to demonstrate that a hyperelastic plate, fabricated with the spatially heterogeneous pre-strains defined by these analytical solutions, can precisely deform into a target shape under its own weight.

To achieve this, we employ an inverse-design methodology. Detailed descriptions of the experimental setup and fabrication process are provided in Appendix C. We first define the target shape for a plate clamped at one end. From this target shape, we calculate the required growth fields based on the derived analytical formulae. This field is engineered to counteract the bending deformation induced by gravitational forces. Using the compatible growth field obtained from our inverse design solution, we numerically simulate the growth process to determine the resulting stress-free configuration. We then fabricated molds corresponding to this specific geometry and cast the silicone samples. Finally, these samples are subjected to gravitational

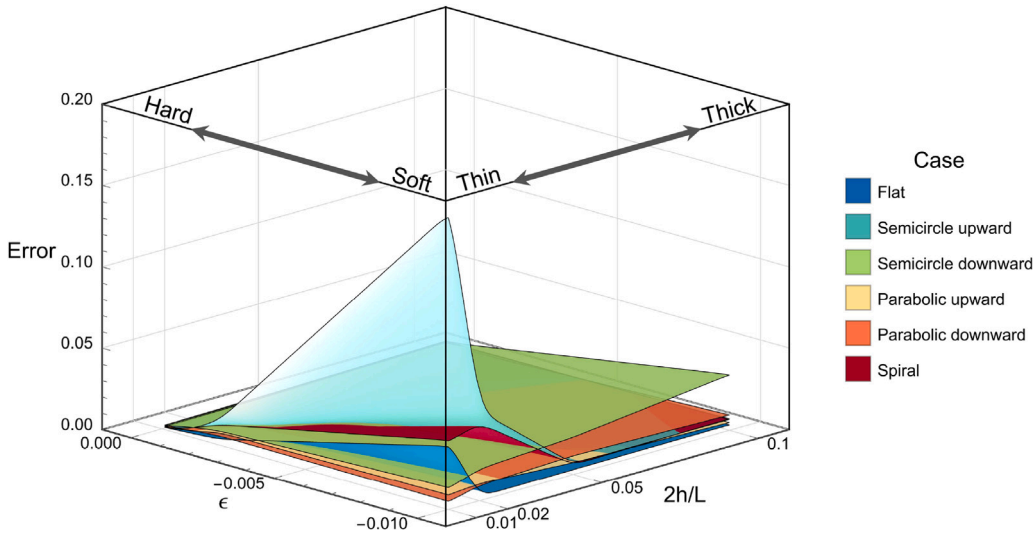


Fig. 9. Error maps of the shape control examples. The 3D surfaces visualize the deviation between the target and simulated shapes across a range of ϵ and slenderness ratios ($2h/L$) for six representative cases. The error metric is calculated based on the root-mean-square error, as defined in Eq. (36).

loading to verify the shape control. Mechanical equilibrium ensures that the plate settles into its intended shape. As illustrated in Fig. 10, the specific steps of this inverse design are detailed as follows

1. Material characterization. The hyperelastic materials used in this experiment are Ecoflex 00-30 and Dragon Skin 20 silicone elastomers (Smooth-On Inc.). To characterize the materials, cylindrical specimens (diameter 30 mm, height 20 mm) are prepared by mixing the liquid components in the prescribed ratio and curing at ambient temperature for 6 h. After curing, the material density ρ_r is determined by weighing. Uniaxial compression tests are performed to obtain the shear modulus C_0, assuming an incompressible neo-Hookean constitutive model.
2. Theoretical design. First, we prescribe the target shape of the plate, characterized by a parametric equation. Using the material parameters determined in the previous step and the parametric equation of the target shape, we compute the required growth functions $\lambda_1^{(0)}(X)$ and $\lambda_1^{(1)}(X)$ via the derived growth function formula, Eq. (25). By implementing these growth functions into the finite element model, the geometry of the grown configuration is obtained through numerical simulation.
3. Sample fabrication. Based on the grown configuration calculated in the previous step, a corresponding mold is fabricated using 3D printing technology. The prepared Ecoflex or Dragon Skin liquid is poured into the mold and allowed to cure at room temperature. Upon demolding, a silicone plate with a specific curvature is obtained.
4. Loading and comparison. The fabricated curved silicone plate is clamped at one end ($X = 0$) in a cantilever setup. The sample is then released, allowing it to deform under its own weight until it reaches a stable equilibrium state. The side profile of the sample is captured and subsequently compared with the target shape to evaluate the accuracy of the theoretical prediction.

Our experiments utilize samples fabricated directly in the grown (stress-free) configuration, rather than samples that are actively grown from a flat state during the experiment. This approach is adopted because precisely controlling a spatially distributed growth field, particularly through-thickness gradients, is experimentally challenging. We emphasize that our framework solves for both the growth gradient $\lambda_1^{(1)}$ (related to curvature) and the bottom surface growth $\lambda_1^{(0)}$ (related to stretching/compression). In many cases, $\lambda_1^{(0)}$ deviates significantly from unity, implying that the sample undergoes substantial elongation or contraction relative to the reference configuration. The term "pre-strained" is thus used to describe this kinematic relationship relative to the reference domain, even though the samples are fabricated in a stress-free state. This indirect realization effectively validates the theoretical design without the need to induce active growth during the loading process. However, a limitation of this approach is that it becomes unavailable when the simulated fully grown configuration is self-intersecting. This makes the grown configuration geometrically incompatible with any manufacturable mold. In such cases, an alternative incremental (e.g., swelling of elastomers) or multilayer growth approach would be required.

Table 2
Experimental settings for six cases.

Case	Target shape	Material	Thickness ($2h$)
1	Flat plate	Ecoflex 00-30	10 mm
2		Dragon Skin 20	10 mm
3		Dragon Skin 20	5 mm
4	Semicircle (downward)	Ecoflex 00-30	10 mm
5		Dragon Skin 20	10 mm
6		Dragon Skin 20	5 mm

Similar to Section 3.3, before conducting the shape programming, we first examine the forward problem of gravity-induced bending in the absence of growth (see Appendix C for details). To generate significant deflection, the material is chosen to be Ecoflex 00-30. The material density ρ_r and shear modulus are obtained from the characterization procedure. Then, these parameters are input into the finite element model to simulate the bending deformation under self-weight loading $\mathbf{b}_r = \rho_r \mathbf{g}$. The predicted deflection profiles closely match experimental measurements (see Fig. C.2), supporting the material characterization, cantilever loading condition, and numerical implementation, and providing a quantitative reference for the subsequent inverse design.

To validate our theoretical framework, we designed six experimental settings, as summarized in Table 2. These cases explore the influence of key factors on shape-control accuracy and effectiveness. We investigate two target shapes: a flat configuration and a downward-bending semicircle. Two different silicone elastomers, Ecoflex 00-30 and Dragon Skin 20, are selected to assess the effect of material properties. Furthermore, samples are fabricated with two different thicknesses, 10 mm and 5 mm, to investigate the role of structural stiffness.

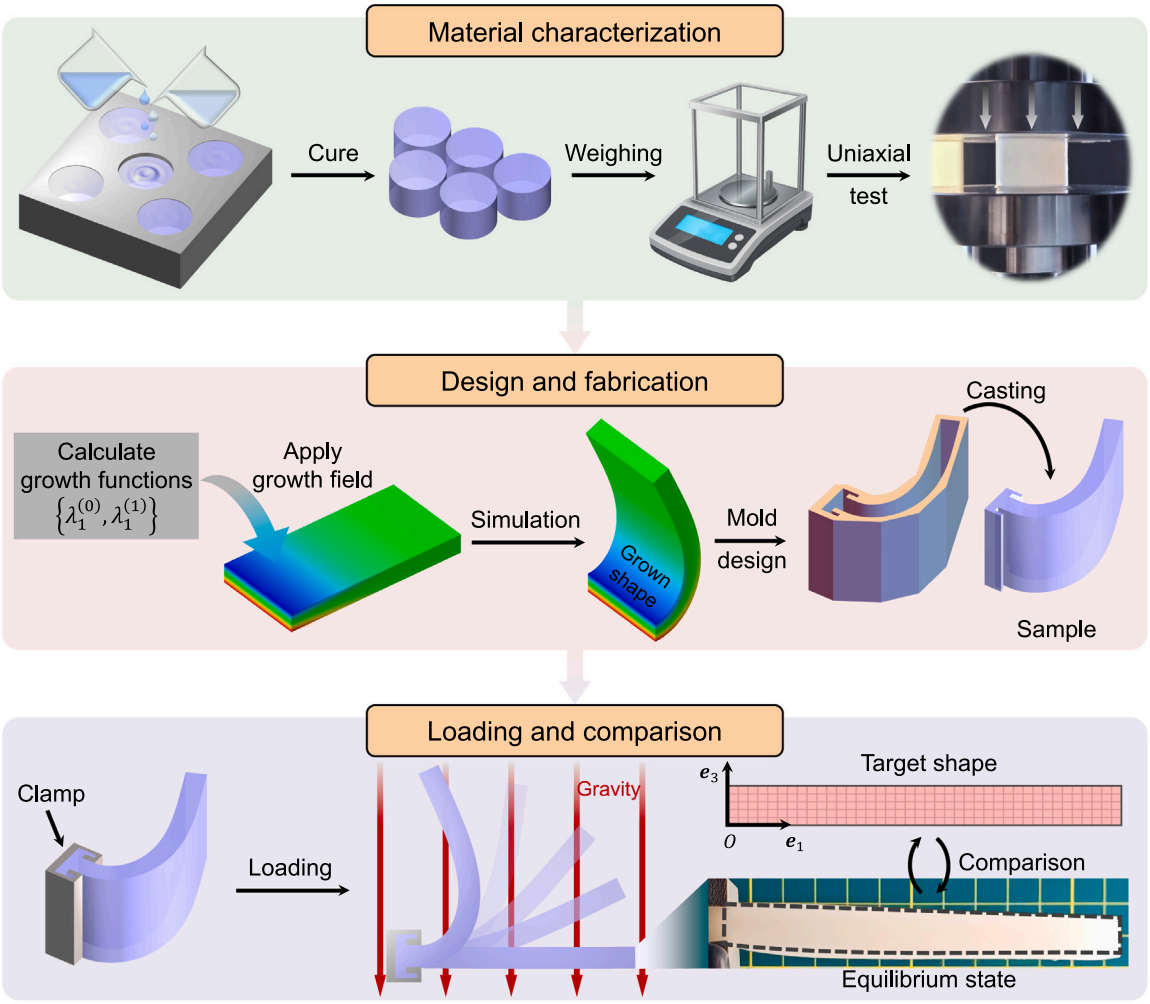


Fig. 10. Workflow for the experimental validation using an inverse-design approach. Step 1: Characterize the density ρ_r and shear modulus C_0 of the silicone elastomers (Ecoflex 00-30 and Dragon Skin 20). Steps 2–3: Calculate the required growth functions analytically, simulate the grown shape, and fabricate the physical sample by casting silicone into a 3D-printed mold that corresponds to the stress-free grown configuration. Step 4: Clamp the sample and release it under gravity. The final equilibrium shape is then compared with the target profile.

Following the characterization procedure, the material properties of the two silicone elastomers are determined. For Ecoflex 00-30, the measured average density ρ_r is $(1.064 \pm 0.005) \times 10^3$ kg/m^3, which is slightly larger than the density of water. Uniaxial compression tests yielded a material parameter C_0 (half of the shear modulus) of $(13.005 \pm 0.379) \times 10^3$ kPa. For Dragon Skin 20 material, the average density is found to be $(1.127 \pm 0.005) \times 10^3$ kg/m^3, and the corresponding material parameter C_0 is determined as $(70.648 \pm 0.719) \times 10^3$ kPa.

The target shapes are defined as a flat configuration for cases 1–3 and a semicircular configuration for cases 4–6. Their bottom surfaces are described by the following parametric equations:

$$\begin{aligned} &\text{Flat plate:} \quad x^{(0)} = X, \quad z^{(0)} = 0, \\ &\text{Semicircle:} \quad x^{(0)} = \frac{1}{20}\sin(10\pi X), \quad z^{(0)} = \frac{1}{20}\left[\cos(10\pi X) - 1\right], \end{aligned} \tag{37}$$

where $X \in [0, L]$.

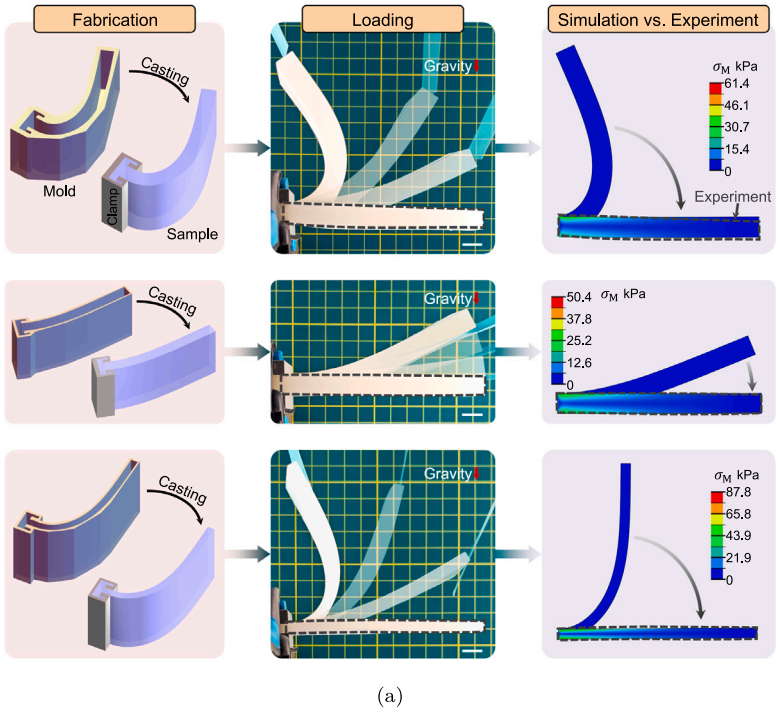
The geometric dimensions of the samples are given by length $L = 0.1$ m and width $W = 0.05$ m, while the thickness $2h$ is either 0.01 m or 0.005 m. Since the value of the gravitational acceleration at the Earth's surface is approximately 9.8 m/s^2, the force per unit mass is $\mathbf{g} = -9.8\mathbf{e}_3$ N/kg. By substituting the material and geometric parameters, and the parametric equations (37) into Eq. (25), we compute the required growth functions $\lambda_1^{(0)}(X)$ and $\lambda_1^{(1)}(X)$ as follows:

$$\begin{aligned} &\text{Flat plate:} \quad \lambda_1^{(0)} = 1 - \frac{15}{4}(1 - 10X)^2\epsilon, \quad \lambda_1^{(1)} = \frac{5}{4}(12000X(5X - 1) + 599)\epsilon, \\ &\text{Semicircle:} \quad \lambda_1^{(0)} = \frac{1}{2}\pi(1 + \epsilon f), \\ &\qquad \lambda_1^{(1)} = \frac{1}{16hL}\Big[\, 160\pi hL + \pi\epsilon(L - X)\sin(10\pi X) \\ &\qquad\qquad + 8\pi(20h - 1)L\epsilon f - 2h\epsilon\cos(10\pi X)\,\Big], \end{aligned} \tag{38}$$

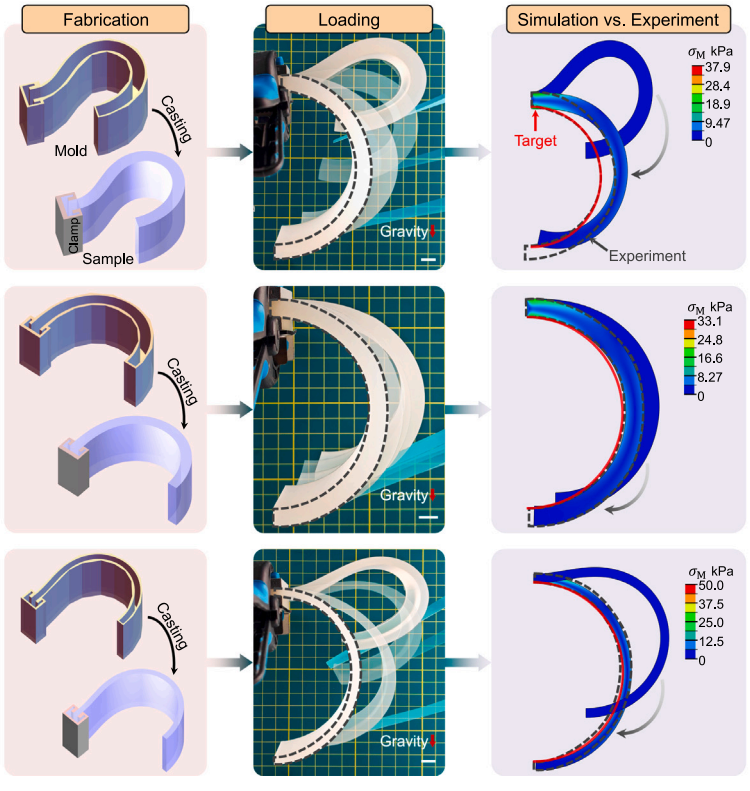
where for the semicircle case, the function f is given by

$$\begin{aligned} f = \frac{1}{1600\pi h(120h - 1)L}\Big[\, &10\pi(40h - 3)(L - X)\sin(10\pi X) \\ &- 3(20h(40h - 1) + 1)(\cos(10\pi L) - \cos(10\pi X))\,\Big]. \end{aligned}$$

The dimensionless parameter $\epsilon = \rho_r L(\mathbf{g} \cdot \mathbf{e}_3)/C_0$ evaluates to $\epsilon \approx -0.08$ for the Ecoflex material and $\epsilon \approx -0.016$ for the Dragon Skin material. Then we build up a finite element model in ABAQUS using the same geometric and material parameters as in the experiment, with boundary conditions set to eliminate rigid body motion. The geometry of the grown configuration is obtained by implementing the growth functions into the finite element model.



(a)



(b)

Fig. 11. Experimental results for shape control under self-weight. (a) Flat target shape. (b) Downward-bending semicircular target shape. The columns show: (left) The fabricated silicone samples; (middle) The deformation process as the support is gradually removed; (right) Comparison of the final experimental profiles (dashed lines) with the target shapes (red solid lines).

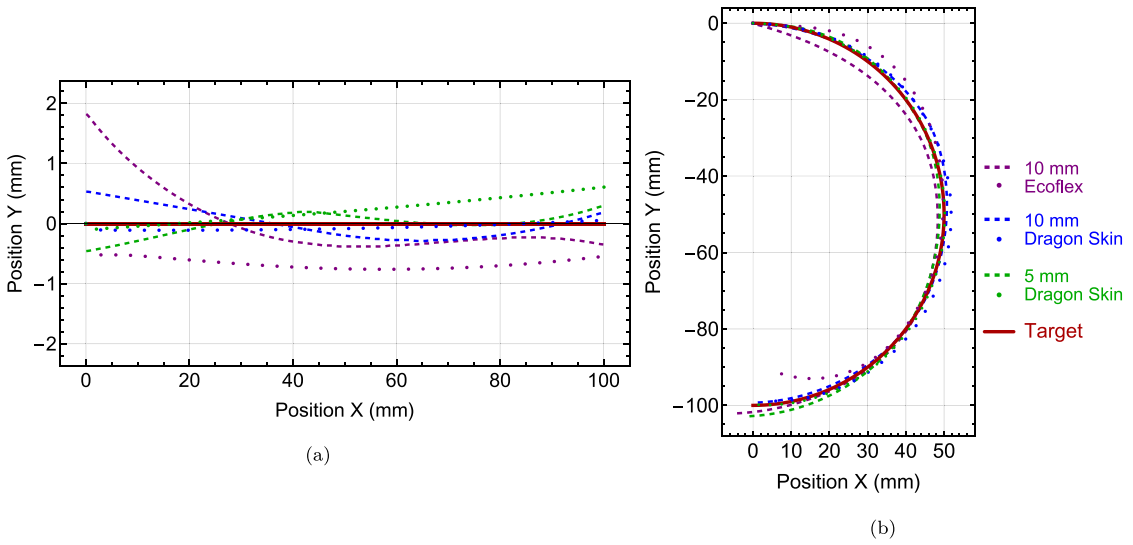


Fig. 12. Discrepancy assessment between the target shapes, finite element simulations, and experiments. The red solid line indicates the theoretical target profile. Scatters denote the equilibrium profile simulated by ABAQUS. Dashed lines represent the experimentally measured profiles extracted from images. Results are shown for two target shapes: (a) flat; (b) downward semicircle.

The mold for fabricating the hyperelastic plate is designed based on the geometry of the grown configuration, and printed using a 3D printer (Bambu Lab P1S). The printed mold is then used to fabricate the hyperelastic plate with a specific curvature by pouring the prepared Ecoflex or Dragon Skin liquid into the mold and allowing it to cure at room temperature for 6 h. The cured plate is then demolded, resulting in a silicone plate with a specific curvature, as shown in the first column of Fig. 11(a) and (b).

The fabricated curved hyperelastic plate is clamped at the left end and free at the right end, forming a cantilever. The sample is then released, allowing it to deform under its own weight until it reaches an equilibrium state. Since gravity cannot be applied gradually, a quasi-static loading protocol is adopted to emulate a smooth application of gravity. A vertical support force is first provided to counterbalance the weight of the free segment and is then withdrawn progressively at a low rate until the plate becomes fully unsupported. In our experiments, the clamped sample is placed on a height-adjustable stage, and a hard paperboard (shown in cyan) gently contacts the bottom surface of the plate. The paperboard is lowered slowly, causing the unconstrained portion to separate from the support and settle into its equilibrium configuration under gravity. The deformation trajectory is visualized in the second column of Fig. 11(a) and (b), where the dashed lines represent the lateral profiles of the plates. The experimental results are compared with the simulation results in the third column of Fig. 11, where the red solid lines delineate the theoretical target shapes of the bottom surface. Additional details on the loading devices are given in Appendix C.

To quantify the discrepancies observed in the validation experiments (Section 4), we evaluate the root-mean-square error in Eq. (36) between the realized bottom profile $\mathbf{r}(X)$ and the theoretical target shape $\mathbf{r}_{\text{target}}(X)$. Fig. 12 presents a detailed comparison for each case, plotting the theoretical profile (red solid line), the simulated equilibrium profile (scatter), and the experimental profile extracted through image processing (dashed line). Based on Eq. (36), $\mathbf{r}$ represents either the simulated result ($\mathbf{r}_{\text{FE}}$), determined by tracking the material coordinates of the mesh, or the experimental result ($\mathbf{r}_{\text{Exp}}$), obtained by sampling points along the deformed profile. The calculated error values (in mm) are summarized in Table 3.

A comparative analysis reveals that, under identical geometric conditions, the stiffer specimens (Dragon Skin 20) exhibit significantly higher fidelity to the target shape compared to the softer ones (Ecoflex 00-30). For a given material, variations in thickness ($2h = 5$ mm versus 10 mm) induce only marginal differences in the final profile. Furthermore, deviations are notably more pronounced for the downward semicircular target than for the flat configuration, which is achieved with sub-millimetre accuracy across both numerical simulations and physical experiments. Overall, the measured profiles closely follow the target shapes, confirming that the preprogrammed growth fields effectively counterbalance the influence of gravity. However, distinct deviations remain, particularly for the softer material (Ecoflex 00-30) in the downward-bending configuration. A detailed discussion on the sources of these discrepancies is provided in Section 5.

5. Discussion

Design principles under body forces

The contrasting growth fields observed in the semicircular examples (Section 3.3) elucidate the fundamental mechanisms governing shape control in the presence of body forces. When the target shape aligns with the gravitational field (e.g., downward bending), the body force acts as an assistive load. Mechanically, this alignment reduces the required growth-induced bending deformations, as gravity naturally drives the plate towards the desired curvature. Consequently, the magnitude of the through-thickness growth gradient $\lambda_1^{(1)}$ is significantly reduced (Fig. 5), leading to lower internal stresses and a stable equilibrium configuration. Conversely, when the target shape opposes gravity (e.g., upward bending), the growth field must generate substantial gradients along the thickness to support the structure against its own weight. This target shape necessitates steep growth gradients and high compressive stresses, which may precipitate structural instabilities. This finding underscores a pivotal design principle in practice: strategically harnessing body forces to assist deformation not only improves energy efficiency by minimizing the required growth actuation but also expands the stable design space.

It is important to distinguish between compensating for passive constraints and utilizing active design variables. While our method modifies the growth field to accommodate unavoidable body forces like gravity, such forces are typically passive environmental constraints rather than controllable inputs. However, the insight gained here implies that controllable body forces—such as electromagnetic or inertial loads—could be actively integrated as primary design variables to

Table 3
Quantitative discrepancy assessment. The simulation error uses $\mathbf{r} = \mathbf{r}_{\mathrm{FE}}$, and the experimental error uses $\mathbf{r} = \mathbf{r}_{\mathrm{Exp}}$. All values are reported in mm.

Case	Target shape	Material	Thickness	Simulation error	Experiment error
1	Flat	Ecoflex 00-30	10 mm	0.67 mm	0.54 mm
2		Dragon Skin 20	10 mm	0.08 mm	0.24 mm
3		Dragon Skin 20	5 mm	0.30 mm	0.17 mm
4	Semicircle (downward)	Ecoflex 00-30	10 mm	5.50 mm	1.72 mm
5		Dragon Skin 20	10 mm	2.72 mm	0.84 mm
6		Dragon Skin 20	5 mm	1.11 mm	1.06 mm

facilitate robust shape morphing. In cases where body forces are negligible ($\epsilon \to 0$), the stress-free shape control methods developed in our previous works [54–57] should be adopted. In such scenarios, introducing artificial body forces is unnecessary, as the stress-free approach inherently offers higher accuracy and stability.

Experimental validation and discrepancies

The experimental results confirm the validity of the inverse design framework, demonstrating that fabricated silicone plates successfully achieve the target flat and curved geometries under self-weight. However, quantitative error analysis (Table 3) reveals noticeable discrepancies, particularly for the softer Ecoflex 00-30 material in the downward-bending configuration. These deviations are likely attributable to three factors extending beyond the idealized hyperelastic model.

First, silicone elastomers exhibit intrinsic viscoelastic behaviour. Despite quasi-static loading, time-dependent creep under self-weight may induce deformations exceeding hyperelastic predictions [83]. This limitation can be addressed by extending the current framework to incorporate viscoelastic constitutive laws, as the general energy formulation (Eq. (6)) accommodates arbitrary material models. Second, the asymptotic theoretical approach may incur higher approximation errors for softer materials (characterized by a larger perturbation parameter ϵ), while fabrication imperfections are also more prone to amplification in these highly compliant structures. Theoretical accuracy can be improved by extending the asymptotic expansion (Eq. (11)) to higher orders (e.g. $O(\epsilon^2)$) to capture complex deformation modes more precisely. Third, experimental boundary conditions deviate from the ideal model, specifically regarding minor compliance at the clamp and the absence of lateral constraints to strictly enforce plane strain. Although theoretical estimates indicate that lateral nominal stresses are negligible ($O(h\epsilon)$), the lack of physical constraints may still contribute to the observed discrepancies. If a stricter lateral constraint is required, it can be realized by clamping the plate on the lateral surfaces or by embedding high-modulus fibres across the width.

Despite these factors, the general agreement between theory and experiment validates the utility of the asymptotic approach for practical soft robotic design.

Operational limits

To define the applicability of our framework, we analyse the error distribution map presented in Fig. 9. The results demonstrate that the inverse design method is robust across a wide range of parameters. However, a distinct operational limit is observed. Specifically, the method fails to converge to the target shape in scenarios combining high gravitational loading (large $|\epsilon|$), extremely low bending stiffness (thin plates), and anti-gravity target shapes (e.g., upward bending). In these regimes, the structure undergoes snap-through instability, a nonlinear bifurcation phenomenon not captured by the first-order asymptotic solution. While the error map empirically identifies this safe operation zone, theoretically deriving the precise stability criterion would require a second-variation (incremental) stability analysis. Since the current framework is built upon a first-order perturbation method to solve the inverse geometric problem, extending it to higher orders to capture these bifurcation points represents a substantial theoretical undertaking that remains beyond the scope of the present study.

6. Conclusions

This work establishes a theoretical framework for programming the shapes of hyperelastic plane-strain plates through differential growth in the presence of body forces. The main findings and contributions are:

- Explicit asymptotic analytical solutions are derived for the inverse problem by introducing a dimensionless parameter ϵ that characterizes the magnitude of the body force. The resulting formulae (25) explicitly relate the geometric quantities (E_r and L_r) of the target shape and the body force to the required growth functions $\lambda_1^{(0)}$ and $\lambda_1^{(1)}$. Unlike iterative numerical optimization or black-box machine learning approaches, these explicit expressions provide direct physical insight into the inverse design problem and facilitate rapid calculation without expensive computational cost.
- A robust two-stage loading strategy is proposed to navigate the nonlinear solution landscape. This method first brings the plate to the stress-free grown target (in the absence of body force) and subsequently applies the body force together with the $O(\epsilon)$ correction of the growth field. This strategy effectively mitigates premature buckling and enables active control of the morphing process, addressing the stability challenges often encountered in gravity-loaded compliant structures.
- Representative numerical examples, including flat, semicircular (up/down), parabolic (up/down), and helical target shapes, are presented under both uniform and linearly varying body forces. The simulated configurations exhibit good agreement with the prescribed target shapes over broad ranges of thickness and ϵ. Experiments using pre-strained silicone plates further validate the shape-control approach for flat and downward-bending semicircular shapes under self-weight.
- The results highlight a concept for utilizing body forces. We demonstrate that body forces are not merely external loads to be resisted but can be strategically harnessed as beneficial factors to assist deformation. This approach can reduce the required growth gradients and expand the stable design space, offering a new paradigm for designing morphing systems under external fields (e.g., gravity, electromagnetic forces).

The proposed framework holds immediate relevance for 4D printing, where the derived spatially varying growth fields ($\lambda_1^{(0)}, \lambda_1^{(1)}$) can be physically realized through programmed printing paths or hydrogel swelling ratios [84,85]. Furthermore, while this study focused on gravity, the theoretical formulation is intrinsically generic and extensible to other body force fields, such as centrifugal forces in aerospace structures or magnetic forces in field-responsive actuators [13,86].

While the proposed framework demonstrates robustness across a wide range of parameters, it is subject to certain limitations as discussed in Section 5. First, the current first-order asymptotic solution does not predict the onset of snap-through instabilities observed in anti-gravity morphing regimes. Second, the purely hyperelastic constitutive

model neglects time-dependent effects such as creep, which contributed to the experimental discrepancies in soft elastomers. Future studies should aim to develop a rigorous stability analysis to identify the theoretical stability boundaries of growth-driven morphing under body forces. Additionally, the framework can be generalized to incorporate more complex constitutive behaviours, such as viscoelasticity, to improve accuracy for real-world soft materials. Finally, the framework offers a foundation for the structural design of metamaterials, provided they can be treated as homogenized continua. In this context, the design of the zeroth-order growth term is analogous to designing in-plane stresses/strains, while higher-order terms govern the bending curvature, thereby unifying the control of stretching and bending. By extending the asymptotic expansion to higher orders, the model can be refined to capture the non-linear through-thickness strain profiles characteristic of such complex architected materials. These advancements will further bridge the gap between theoretical growth mechanics and the engineering of robust, force-adaptive morphing structures.

CRediT authorship contribution statement

Zhanfeng Li: Writing – original draft, Visualization, Validation, Methodology, Investigation, Funding acquisition. **Xiaohu Yao:** Writing – review & editing, Project administration, Methodology, Investigation, Conceptualization. **Mokarram Hossain:** Writing – review & editing, Project administration, Methodology, Investigation, Funding acquisition, Conceptualization. **Jiong Wang:** Writing – review & editing, Supervision, Project administration, Methodology, Investigation, Conceptualization.

Declaration of competing interest

The authors declare that they have no known competing financial interests or personal relationships that could have appeared to influence the work reported in this paper.

Acknowledgements

Z.L. gratefully acknowledges support from the Postdoctoral Innovation Talent Support Program of China (No.: BX20240119), Guangdong Basic and Applied Basic Research Foundation (Project No. : 2025A1515010680), and the China Postdoctoral Science Foundation, China under Grant Number 2025M771845. M.H. acknowledges the support of the EPSRC, United Kingdom via a Standard Grant (EP/Z535710/1) and the Royal Society (UK) through the International Exchange Grant (IEC/NSFC/211316).

Appendix A. Sensitivity analysis of loading paths

To assess the robustness of the proposed shape-control framework, we investigated the sensitivity of the final equilibrium shape to the sequence of loading. We considered four loading paths mentioned in Section 3.2:

- **Path-i:** The body force (gravity) is applied first to the reference plate, followed by the activation of the growth field.
- **Path-ii:** The growth field is applied first to generate the fully grown shape, followed by the application of the body force.
- **Path-iii:** Both the body force and the growth field are increased proportionally and simultaneously from initial to their final values.
- **Path-iv:** The two-stage path proposed in this work. Stage I applies the base growth field $\mathbb{G}_0$ to reach the stress-free target shape (intermediate state). Stage II simultaneously applies the body force and the growth correction term to reach the final configuration (fully grown).

We performed finite element simulations for three representative cases with varying thickness ($2h$) and body force intensity (ϵ), as shown in Fig. A.1. The results demonstrate a clear dependence on the loading path. For all cases, path-i and path-iii fail to reach the target shape, likely due to premature buckling or settling in unexpected equilibrium branches. In contrast, both path-ii and path-iv can generate the desired configurations for cases 2 and 3 (moderate conditions). However, for the extreme scenario of case 1 (thin plate, large body force), path-ii becomes problematic. The growth field required to compensate for strong gravity induces bending deformations. Applying this field without the counteracting body force (stage I of path-ii) causes the plate to curl into a complex, self-contacting spiral (see Fig. A.1, case 1). This curly state prevents the correct application of gravity in the subsequent step. Although realizing the exact target shape in case 1 remains challenging for all paths due to the extreme parameters, the proposed path-iv exhibits the most robust behaviour. By targeting the simple stress-free shape first and then introducing gravity and compensation simultaneously, it avoids the chaotic intermediate states of path-ii while maintaining the convergence capability seen in cases 2 and 3. Therefore, the proposed loading strategy offers the best balance of versatility and robustness.

Appendix B. Mesh convergence test

Before conducting the shape-control simulations in Section 3.3, we perform a mesh sensitivity analysis to determine an efficient and accurate discretization strategy. We consider a cantilever plate undergoing large pure-bending deformation under gravity, corresponding to the forward problem without growth. To ensure the robustness of the numerical results, we select the most extreme geometric case considered in this study: a plate with length $L = 1$ m and thickness $2h = 0.01$ m (aspect ratio $L/2h = 100$). This configuration represents the thinnest specimen, which is most susceptible to mesh-dependent errors. Consequently, establishing convergence for this limiting case ensures the validity of the discretization for all other thicker samples ($L/2h < 100$) used in the simulations. The density is set to $\rho_r = 1000\ \mathrm{kg/m^3}$, and the plate is clamped at $X = 0$. The body force is taken as a uniform gravity load $\mathbf{b}_r = -10\,\mathbf{e}_3\ \mathrm{N/m^3}$, and the neo-Hookean material parameter is chosen as $C_0 = 0.5 \times 10^6$ Pa.

To assess the influence of the through-thickness discretization, five meshes are generated by dividing the thickness direction into $N_z = 1, 2, 4, 6$, and 8 elements, respectively. In each case, the in-plane element size is maintained as close to square as possible by setting the number of elements along the length to $N_x = L/(2h/N_z) = 100N_z$, so that the typical element size is

$$\Delta x \approx \Delta z \approx \frac{2h}{N_z} = \frac{0.01}{N_z}\ \mathrm{m},$$

giving $\Delta x = 0.01, 0.005, 0.0025, 0.00167$, and 0.00125 m for $N_z = 1, 2, 4, 6$, and 8, respectively. For each mesh, the static equilibrium configuration under self-weight is computed, and the vertical tip displacement as well as the stress distribution are recorded.

As shown in Fig. B.1(a), the vertical tip displacement converges rapidly with increasing number of elements through the thickness. The relative errors with respect to the reference solution ($N_z = 10$) are labelled. For the coarsest mesh with $N_z = 1$, the tip displacement deviates visibly from the converged value. Refinement to $N_z = 2$ reduces the relative error to 0.047%, and further refinement to $N_z = 4$ brings the error down to 0.010%. For $N_z = 6$ and $N_z = 8$, the errors are negligible (0.003% and 0.001%, respectively), indicating that the solution is essentially mesh-independent in this range. Moreover, Fig. B.1(b) displays the von Mises stress distribution near the clamped end. The contours confirm that the mesh with six elements through the thickness ($N_z = 6$) already captures the smooth stress variation accurately, avoiding stress discontinuities observed in the coarser meshes (e.g., $N_z = 1$ and $N_z = 2$). Based on these observations, a discretization

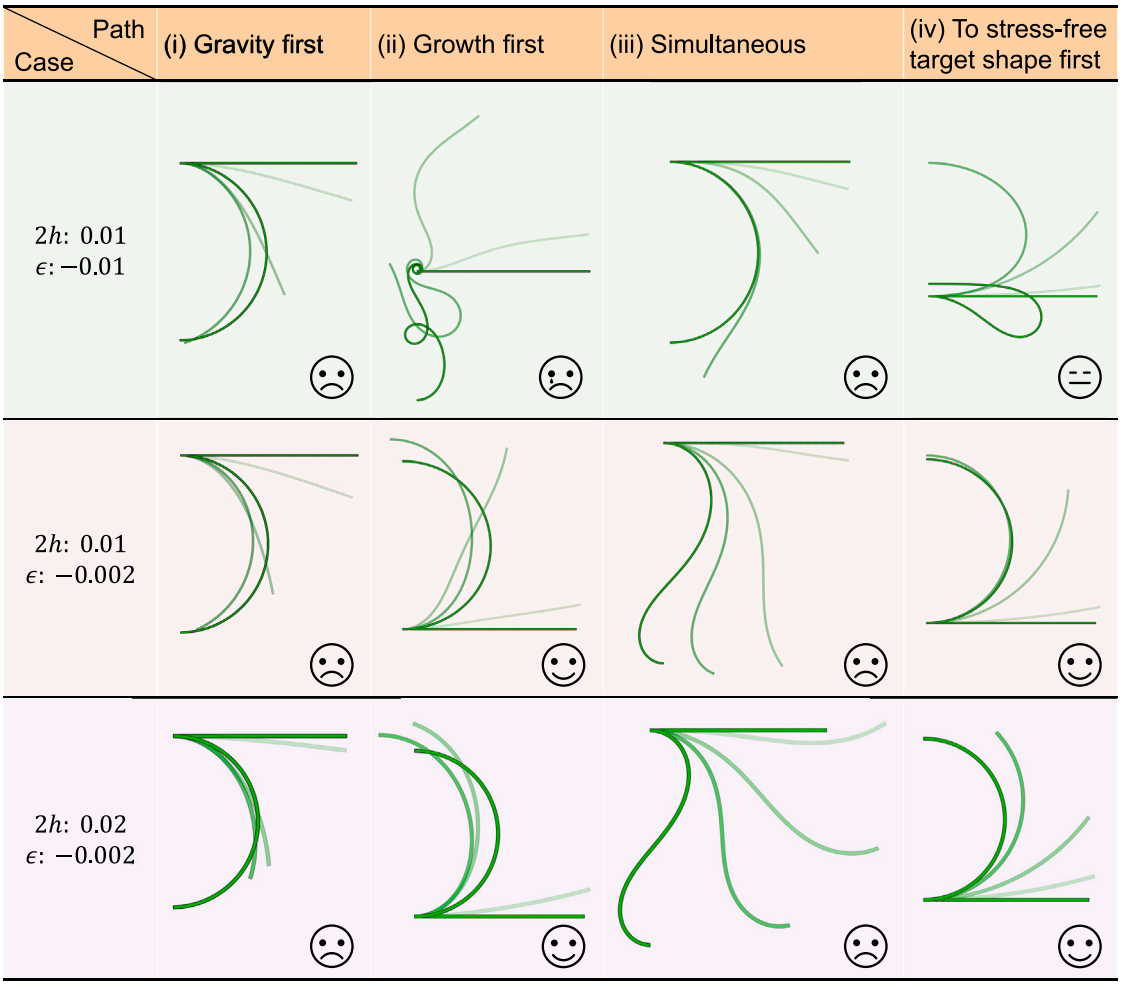


Fig. A.1. Sensitivity analysis of the loading path. Comparison of the deformation process and final shapes obtained under four different loading sequences for three cases. Path-i and path-iii fail to reach the target shape in all cases. Path-ii succeeds in cases 2 and 3 but leads to a chaotic spiral in the extreme case 1. The proposed path-iv proves to be the most robust strategy, succeeding in cases 2 and 3 and avoiding the chaotic intermediate state in case 1.

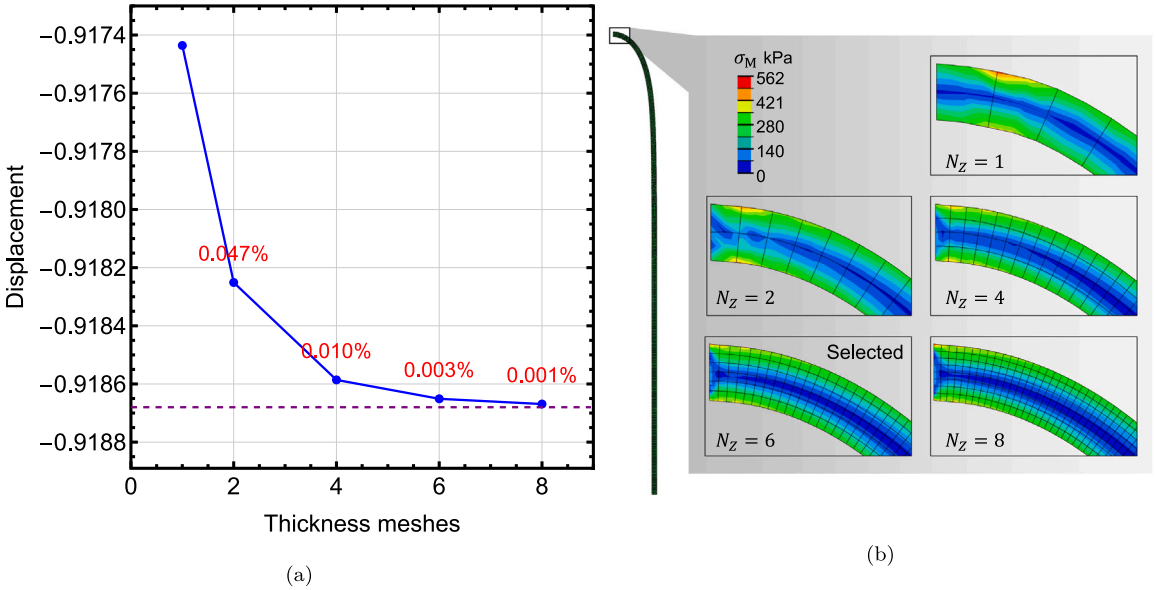
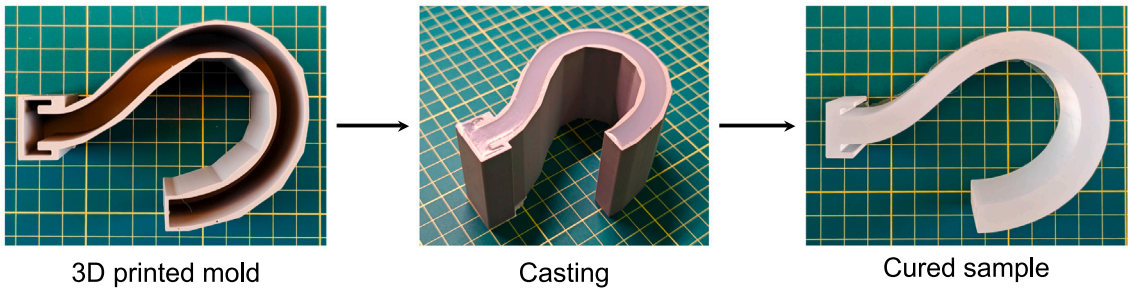
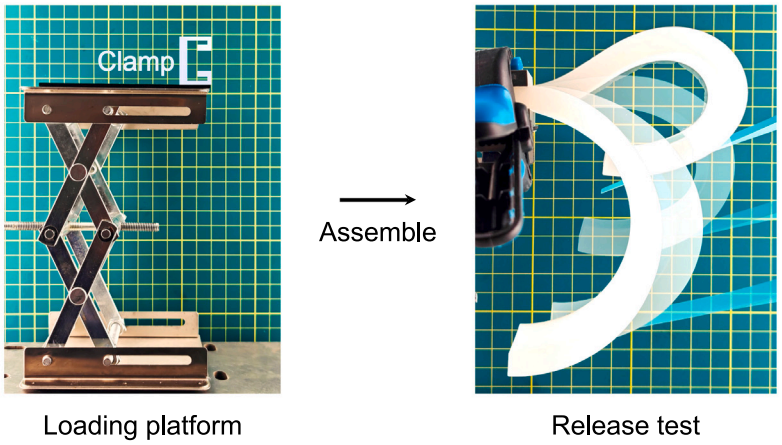


Fig. B.1. Mesh convergence study for the gravity-induced bending of a cantilever plate with $L = 1$ m and $2h = 0.01$ m. (a) Vertical tip displacement (u_X) versus the number of elements through the thickness N_z. The relative errors with respect to the reference solution ($N_z = 10$, dashed line) are labelled. (b) Comparison of von Mises stress distributions near the clamped end for different mesh densities.



(a)



(b)

Fig. C.1. Experimental implementation details. (a) Fabrication workflow showing the 3D-printed mold, the casting process, and the cured sample. (b) Testing procedure illustrating the loading platform, the sample assembly, and the release test for gravity application.

with six elements through the thickness ($N_z = 6$) and 600 elements along the length is adopted in subsequent finite-element simulations. For thicker plates, the number of elements through the thickness is adjusted proportionally to maintain a similar element aspect ratio. Since the selected benchmark represents the most critical case, this discretization strategy guarantees sufficient accuracy for simulations presented in this work.

Appendix C. Experimental details

Experimental setups

To provide further clarity on the experimental implementation, detailed views of the fabrication and testing apparatus are presented in Fig. C.1.

Fig. C.1(a) illustrates the fabrication workflow. The process begins by determining the geometry of the target stress-free configuration through finite element simulation, incorporating the calculated growth fields. The surface coordinates of this simulated shape are exported and reconstructed in the 3D modelling software `Blender`. Based on this reference geometry, a mold is designed. The multi-part molds are manufactured using a Fused Deposition Modelling (FDM) 3D printer (Bambu Lab P1S) with Polylactic Acid (PLA) filament. These molds are designed with detachable components to facilitate the demolding of curved silicone samples without inducing plastic deformation. The liquid silicone elastomers (Ecoflex 00-30 and Dragon Skin 20, Smooth-On Inc.) are prepared, degassed, and cast into these molds. After curing at room temperature for 6 h, the samples with the prescribed stress-free shapes are obtained.

Fig. C.1(b) depicts the testing procedure. A custom experimental setup featuring a height-adjustable scissor lift is employed. The sample is first clamped at the fixed boundary ($X = 0$), while the suspended portion is supported by a platform. Subsequently, the support is gradually lowered to perform the quasi-static release test, ensuring that the gravitational loading is applied smoothly until the plate reaches its equilibrium state.

Pure bending benchmark example

As discussed in Section 4, before implementing the complex inverse design for shape control, it is essential to validate the predictive capability of our numerical framework on a simpler forward problem. This benchmark case serves to (i) establish a quantitative baseline of gravity-only deformation for the given geometry and materials, ensuring that the finite element model correctly captures the large-deformation mechanics under self-weight; (ii) validate the fidelity of the material characterization (density ρ_r and shear modulus C_0) and the experimental boundary conditions (clamping effectiveness) against laboratory measurements; and (iii) capture the magnitude of gravity-induced deflection to inform the subsequent inverse design, confirming that the chosen material is sufficiently compliant to exhibit significant gravitational effects. In this benchmark case, the silicone cantilever plate is clamped at the left end ($X = 0$). The geometric dimensions of the silicone plate are defined as $L \times W \times 2h = 100\ \text{mm} \times 50\ \text{mm} \times 10\ \text{mm}$. To generate significant deflection, the material is chosen to be Ecoflex 00-30. The material density ρ_r and shear modulus (i.e., $2C_0$ for a neo-Hookean solid) are obtained from the characterization procedure. Then, these parameters are input into the finite element model to simulate the bending deformation under self-weight loading $\mathbf{b}_r = \rho_r \mathbf{g}$. The simulated deflected profiles are compared with experimental measurements (see Fig. C.2). The experimental deflection profile almost coincides with the simulated results, validating the characterization of material parameters and boundary condition implementation, which helps establish a reliable workflow for the subsequent inverse growth-field design.

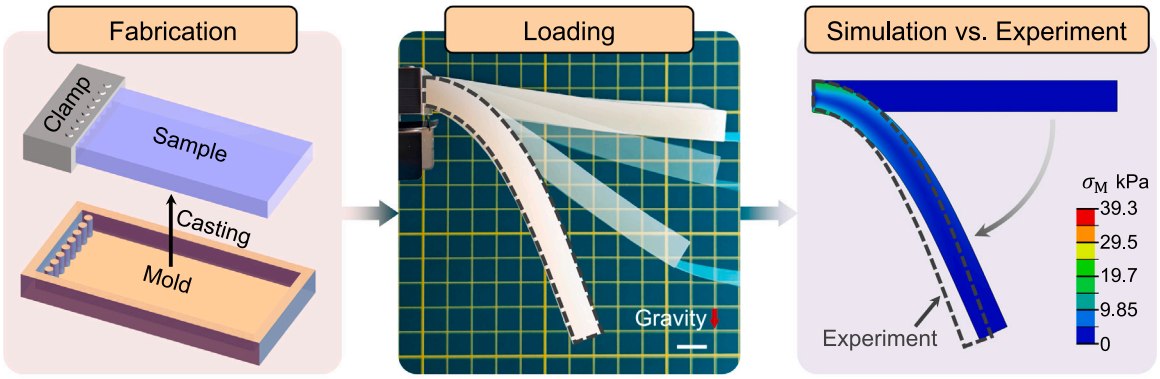


Fig. C.2. Gravity-induced bending of a pure Ecoflex 00-30 plate without growth. The experimental deflection profile (grey dashed line) closely matches the finite element simulation.

Appendix D. Supplementary data

Supplementary material related to this article can be found online at https://doi.org/10.1016/j.ijmecsci.2026.111329.

Movie 1: The experimental/simulated deforming process of the examples shown in Section 4.

Data availability

Data will be made available on request.

References

[1] Ambrosi D, Ateshian GA, Arruda EM, Cowin SC, Dumais J, Goriely A, Holzapfel GA, Humphrey JD, Kemkemer R, Kuhl E. Perspectives on biological growth and remodeling. J Mech Phys Solids 2011;59(4):863–83.

[2] Goriely A. The mathematics and mechanics of biological growth, vol. 45, Springer; 2017.

[3] Ambrosi D, Ben Amar M, Cyron CJ, DeSimone A, Goriely A, Humphrey JD, Kuhl E. Growth and remodelling of living tissues: Perspectives, challenges and opportunities. J R Soc Interface 2019;16(157):20190233.

[4] Huang C, Wang Z, Quinn D, Suresh S, Hsia KJ. Differential growth and shape formation in plant organs. Proc Natl Acad Sci USA 2018;115(49):12359–64.

[5] Smithers ET, Luo J, Dyson RJ. Mathematical principles and models of plant growth mechanics: From cell wall dynamics to tissue morphogenesis. J Exp Bot 2019;70(14):3587–600.

[6] Liu C, Wang F, Tao W, Lü C. Geometrical incompatibility regulated pattern selection and morphological evolution in growing spherical soft tissues. Int J Mech Sci 2024;284:109720.

[7] Zhang Y, Cohen OY, Moshe M, Sharon E. Geometrically frustrated rose petals. Science 2025;388(6746):520–4.

[8] Tang J, Chen Z, Cai Y, He J, Luo Y. Stretch-Activated reprogrammable Shape-Morphing composite elastomers. Adv Funct Mater 2022;32(34):2203308.

[9] Li B, Cao Y-P, Feng X-Q, Gao H. Mechanics of morphological instabilities and surface wrinkling in soft materials: A review. Soft Matter 2012;8(21):5728.

[10] Rausch MK, Kuhl E. On the mechanics of growing thin biological membranes. J Mech Phys Solids 2014;63:128–40.

[11] Wang Q, Ghrayeb A, Kim S, Cheng L, Tawfick S. The mechanics and physics of twisted and coiled polymer actuators. Int J Mech Sci 2024;280:109440.

[12] Liu C, Du Y, Li K, Han Z, Lü C. Growth and morphogenesis of an everted tubular biological tissue. Proc R Soc A: Math Phys Eng Sci 2024;480(2283):20230816.

[13] Wang Y, Li Z, Chen X, Tan Y, Wang F, Du Y, Zhang Y, Su Y, Xu F, Wang C, Chen W, Liu J. Electroactive differential growth and delayed instability in accelerated healing tissues. J Mech Phys Solids 2024;193:105867.

[14] Soleyman E, Aberoumand M, Rahmatabadi D, Soltanmohammadi K, Ghasemi I, Baniassadi M, Abrinia K, Baghani M. Assessment of controllable shape transformation, potential applications, and tensile shape memory properties of 3D printed PETG. J Mater Res Technol 2022;18:4201–15.

[15] Mirasadi K, Yousefi MA, Jin L, Rahmatabadi D, Baniassadi M, Liao W-H, Bodaghi M, Baghani M. 4D printing of magnetically responsive shape memory polymers: Toward sustainable solutions in soft robotics, wearables, and biomedical devices. Adv Sci 2025;n/a(n/a):e13091.

[16] Zhang C, Yang H, Garziera R, Xu Y, Jiang H. Reprogrammable gripper through pneumatic tunable bistable origami actuators. Int J Mech Sci 2025;286:109889.

[17] Kondaurov V, Nikitin L. Finite strains of viscoelastic muscle tissue. J Appl Math Mech 1987;51(3):346–53.

[18] Takamizawa K, Hayashi K. Strain energy density function and uniform strain hypothesis for arterial mechanics. J Biomech 1987;20(1):7–17.

[19] Rodriguez EK, Hoger A, McCulloch AD. Stress-dependent finite growth in soft elastic tissues. J Biomech 1994;27(4):455–67.

[20] Sadik S, Yavari A. On the origins of the idea of the multiplicative decomposition of the deformation gradient. Math Mech Solids 2017;22(4):771–2.

[21] Boedec G, Deschamps J. Disk wrinkling under gravity. Int J Solids Struct 2021;233:111214.

[22] Liu C, Du Y, Li K, Lü C. Morphological instability of geometrically incompatible bilayer tubes. Int J Mech Sci 2024;269:109061.

[23] Ben Amar M. Wrinkles, creases, and cusps in growing soft matter. Rev Modern Phys 2025;97(1):015004.

[24] Li Q, Healey TJ. Stability boundaries for wrinkling in highly stretched elastic sheets. J Mech Phys Solids 2016;97:260–74.

[25] Steigmann DJ. Koiter's shell theory from the perspective of Three-dimensional nonlinear elasticity. J Elasticity 2013;111(1):91–107.

[26] Dai H-H, Song Z. On a consistent Finite-Strain plate theory based on three-dimensional energy principle. Proc R Soc A: Math Phys Eng Sci 2014;470(2171):20140494.

[27] Wang T, Yang Y, Xu F. Mechanics of tension-induced film wrinkling and restabilization: A review. Proc R Soc A: Math Phys Eng Sci 2022;478(2263):20220149.

[28] Wang J, Steigmann D, Wang F-F, Dai H-H. On a consistent Finite-Strain plate theory of growth. J Mech Phys Solids 2018;111:184–214.

[29] Du P, Wang J, Li Z, Cai W. On a Finite-Strain plate theory for Growth-Induced plane-strain deformations and instabilities of Multi-Layered hyperelastic plates. Int J Solids Struct 2022;236–237:111348.

[30] Niu Y, Chen Y, Zhao T, Jin G, Zhang G, Fan Y. Transverse vibration of plate with multiple curved through cracks. Int J Mech Sci 2024;274:109293.

[31] Sharon E, Efrati E. The mechanics of Non-euclidean plates. Soft Matter 2010;6(22):5693–704.

[32] Pezzulla M, Stoop N, Jiang X, Holmes DP. Curvature-Driven morphing of Non-euclidean shells. Proc R Soc A: Math Phys Eng Sci 2017;473(2201):20170087.

[33] Altenbach J, Altenbach H, Eremeyev VA. On generalized Cosserat-type theories of plates and shells: A short review and bibliography. Arch Appl Mech 2010;80(1):73–92.

[34] Pruchnicki E. Homogenization of nonlinear Cosserat plate including growth theory when the thickness of the plate and the size of the in-plane heterogeneities are of the same order of magnitude. Math Mech Solids 2024;29(10):1999–2015.

[35] Bickley W. The heavy elastica. Lond Edinb Dublin Philos Mag J Sci 1934;17(113):603–22.

[36] Lü C, Sun C, Cai S. Mechanics and physics under supergravity conditions. Acta Mech Sin 2024;40(6):724902.

[37] Romero V, Ly M, Rasheed AH, Charrondière R, Lazarus A, Neukirch S, Bertails-Descoubes F. Physical validation of simulators in computer graphics. ACM Trans Graph 2021;40(4):1–19.

[38] Endo T, Kawasaki H. Bending moment-based force control of flexible arm under gravity. Mech Mach Theory 2014;79:217–29.

[39] Shah R, van der Heijden GHM. Buckling and Lift-off of a heavy rod compressed into a cylinder. J Mech Phys Solids 2024;182:105464.

[40] Curtis GK, Griffiths IM, Vella D. Bridging a gap: A heavy elastica between point supports. Int J Solids Struct 2026;326:113702.

[41] Azarniya O, Forooghi A, Bidhendi MV, Zangoei A, Naskar S. Exploring buckling and post-buckling behavior of incompressible hyperelastic beams through innovative experimental and computational approaches. Mech Based Des Struct Mach 2024;52(7):4791–810.

[42] Forte AE, Hanakata PZ, Jin L, Zari E, Zareei A, Fernandes MC, Sumner L, Alvarez J, Bertoldi K. Inverse design of inflatable soft membranes through machine learning. Adv Funct Mater 2022;32(16):2111610.
[43] Biswas S, Yashin VV, Balazs AC. Biomimetic growth in polymer gels. Mater Horiz 2024;11(1):163–72.
[44] Yang Y, Dai Z, Chen Y, Xu F. Active twisting for adaptive droplet collection. Nat Comput Sci 2025;5(4):313–21.
[45] van Rees WM, Vouga E, Mahadevan L. Growth patterns for Shape-Shifting elastic bilayers. Proc Natl Acad Sci 2017;114(44):11597–602.
[46] Ortigosa-Martínez R, Martínez-Frutos J, Mora-Corral C, Pedregal P, Periago F. Shape-Programming in hyperelasticity through differential growth. Appl Math Optim 2024;89(2):49.
[47] Bertails-Descoubes F, Derouet-Jourdan A, Romero V, Lazarus A. Inverse design of an isotropic suspended Kirchhoff rod: Theoretical and numerical results on the uniqueness of the natural shape. Proc R Soc A: Math Phys Eng Sci 2018;474(2212):20170837.
[48] Chen X, Zheng C, Xu W, Zhou K. An asymptotic numerical method for inverse elastic shape design. ACM Trans Graph 2014;33(4):1–11.
[49] Luo K, Zhao J, Wang Y, Li J, Wen J, Liang J, Soekmadji H, Liao S. Physics-informed neural networks for PDE problems: A comprehensive review. Artif Intell Rev 2025;58(10):323.
[50] Ahmed AH, Mzili M, Torki M, Benlalia Z, Hankar M, Abatal A, Mzili T. Structural insights into bracket behavior: A statistical and displacement-stress analysis. Mesop J Civ Eng 2025;2025:38–48.
[51] Lu L, Pestourie R, Yao W, Wang Z, Verdugo F, Johnson SG. Physics-informed neural networks with hard constraints for inverse design. SIAM J Sci Comput 2021;43(6):B1105–32.
[52] Han X-Q, Wang X-D, Xu M-Y, Feng Z, Yao B-W, Guo P-J, Gao Z-F, Lu Z-Y. AI-Driven inverse design of materials: Past, present, and future. Chin Phys Lett 2025;42(2):027403.
[53] Feng J, Qiao J, Xu Q, Zhang G, Li L. Accelerated design of Acoustic-Mechanical multifunctional metamaterials via neural network. Int J Mech Sci 2025;287:109920.
[54] Wang J, Li Z, Jin Z. A theoretical scheme for Shape-Programming of thin hyperelastic plates through differential growth. Math Mech Solids 2022;27(8):1412–28.
[55] Li Z, Wang J, Hossain M, Kadapa C. A general theoretical scheme for Shape-Programming of incompressible hyperelastic shells through differential growth. Int J Solids Struct 2023;265:112128.
[56] Wang J, Jin Z, Li Z. Realization of planar and surface conformal mappings through Stress-Free growth of hyperelastic plates: Analytical formulas and numerical calculations. J Mech Phys Solids 2024;190:105727.
[57] Li Z, Wang J. General shape transformations of thin hyperelastic shells through Stress-Free differential growth. Internat J Engrg Sci 2025;213:104266.
[58] Chen X, Shen Y, Li Z, Gu D, Wang J. Generating complex fold patterns through stress-free deformation induced by growth. J Mech Phys Solids 2022;159:104702.
[59] Li J, Huang W, Zhu Y, Yu L, Sun X, Liu M, Wu H. Inverse elastica: A theoretical framework for inverse design of morphing slender structures. J Mech Phys Solids 2026;208:106488.
[60] Amiri Delouei A, Emamian A, Ghorbani S, Khorrami A, Jafarian K, Sajjadi H, Atashafrooz M, Jing D, Tarokh A. A review on analytical heat transfer in functionally graded materials, Part I: Fourier heat conduction. J Therm Sci 2025;34(4):1358–86.
[61] Amiri Delouei A, Emamian A, Ghorbani S, Khorrami A, Jafarian K, Sajjadi H, Atashafrooz M, Jing D, Tarokh A. A review on analytical heat transfer in functionally graded materials, Part II: Non-Fourier heat conduction. J Therm Sci 2025;34(4):1387–407.
[62] Lü C, Li K, Du Y, Zhang H, Liu C, Zhan H. Harnessing Gravity-Induced instability of soft materials: Mechanics and application. Adv Funct Mater 2024;34(30):2314255.
[63] Liu T, Wang X. Inverse design of Three-Dimensional variable curvature pneumatic soft actuators. J Mech Robot 2025;17(071004).
[64] Tao B, Luo K, Tian Q, Hu H. Inverse dynamic design for motion control of soft machines driven by dielectric elastomer actuators. Int J Mech Sci 2024;273:109213.
[65] Wang Y, Zhao Y, Tian Y, Cao D, Yang Z. Improving the Gravity-Rotation-Excited vibration energy harvesting in offset configurations. Int J Mech Sci 2023;243:108033.
[66] Ben Amar M, Goriely A. Growth and instability in elastic tissues. J Mech Phys Solids 2005;53(10):2284–319.
[67] Steinmann P. Views on multiplicative elastoplasticity and the continuum theory of dislocations. Internat J Engrg Sci 1996;34(15):1717–35.
[68] Erlich A, Zurlo G. Incompatibility-driven growth and size control during development. J Mech Phys Solids 2024;188:105660.
[69] Dervaux J, Amar MB. Morphogenesis of growing soft tissues. Phys Rev Lett 2008;101(6):068101.
[70] Kadapa C, Li Z, Hossain M, Wang J. On the advantages of mixed formulation and Higher-Order elements for computational morphoelasticity. J Mech Phys Solids 2021;148:104289.
[71] Wang J, Wang Q, Dai H-H, Du P, Chen D. Shape-programming of hyperelastic plates through differential growth: An analytical approach. Soft Matter 2019;15(11):2391–9.
[72] Hossain M, Steinmann P. More hyperelastic models for Rubber-like materials: Consistent tangent operators and comparative study. J Mech Behav Mater 2013;22(1–2):27–50.
[73] Mihai LA, Budday S, Holzapfel GA, Kuhl E, Goriely A. A family of hyperelastic models for human brain tissue. J Mech Phys Solids 2017;106:60–79.
[74] Ciarletta P, Ben Amar M. Growth instabilities and folding in tubular organs: A variational method in Non-Linear elasticity. Int J Non-Linear Mech 2012;47(2):248–57.
[75] Yu X, Fu Y, Dai H-H. A refined dynamic Finite-Strain shell theory for incompressible hyperelastic materials: Equations and Two-Dimensional shell virtual work principle. Proc R Soc A: Math Phys Eng Sci 2020;476(2237):20200031.
[76] Feng T, Chen J, Wong J-W, Li S, Miao Z, Wang Z, Li X, Cao J, Xue Y, Yang X, Liu M, Li T. Twist-Induced bifurcation and path manipulation in compressed ribbons. J Mech Phys Solids 2026;206:106328.
[77] Abe T, Hashiguchi I, Nakahara Y, Kobayashi S, Tarumi R, Takahashi H, Ishigami G, Sano TG. Snap and jump: How elastic shells pop out. Adv Robot Res 2025;1(2):202500041.
[78] Wang W, Li C, Cho M, Ahn S-H. Soft Tendril-Inspired grippers: Shape morphing of Programmable Polymer–Paper bilayer composites. ACS Appl Mater Interfaces 2018;10(12):10419–27.
[79] Abdulbaqi AS, Alsultan QH, Nejrs SM, Alla IHA, khalaf Jabur Y, Jassim SA, kareem Mohammed M, Sulaiman BH, deen Shawqi OSA, jasim Mohameed O, Abed TH, Panessai IY, Khalaf HA. Design and fabrication of bio-inspired robotic systems for developed mobility and functionality in unstructured environments. Khwarizmia 2023;2023:46–62.
[80] Li L, He S, Qi Q, Zeng J, Kang S, Endo G, Nabae H, Ma S, Suzumori K. PEGrip: A Plant-Tendril-Inspired passive entanglement gripper enabling Fail-Safe grasping. IEEE Robot Autom Lett 2024;9(8):7039–46.
[81] Li Y, Zhang Q, Li K, Feng J, Cai J, Laschi C. Modular soft origami pneumatic actuator (SOPA) with tunable stiffness. Int J Mech Sci 2025;305:110721.
[82] Gayed RB, Ghali A. Control of Long-Term deflection of concrete slabs by prestressing. Struct Concr 2019;20(6):1816–27.
[83] Xiang Y, Zhong D, Wang P, Yin T, Zhou H, Yu H, Baliga C, Qu S, Yang W. A physically based Visco-Hyperelastic constitutive model for soft materials. J Mech Phys Solids 2019;128:208–18.
[84] Ren L, Li B, Wang K, Zhou X, Song Z, Ren L, Liu Q. Plant-Morphing strategies and Plant-Inspired soft actuators fabricated by biomimetic our-Dimensional printing: A review. Front Mater 2021;8:651521.
[85] Li H, Bartolo PJDS, Zhou K. Direct 4D printing of hydrogels driven by structural topology. Virtual Phys Prototyp 2025;20(1):e2462962.
[86] Li Z, Wang Y, Wang Z, Kadapa C, Hossain M, Yao X, Wang J. Coupled Magneto-Mechanical growth in hyperelastic materials: Surface patterns modulation and shape control in Bio-Inspired structures. J Mech Phys Solids 2025;200:106089.